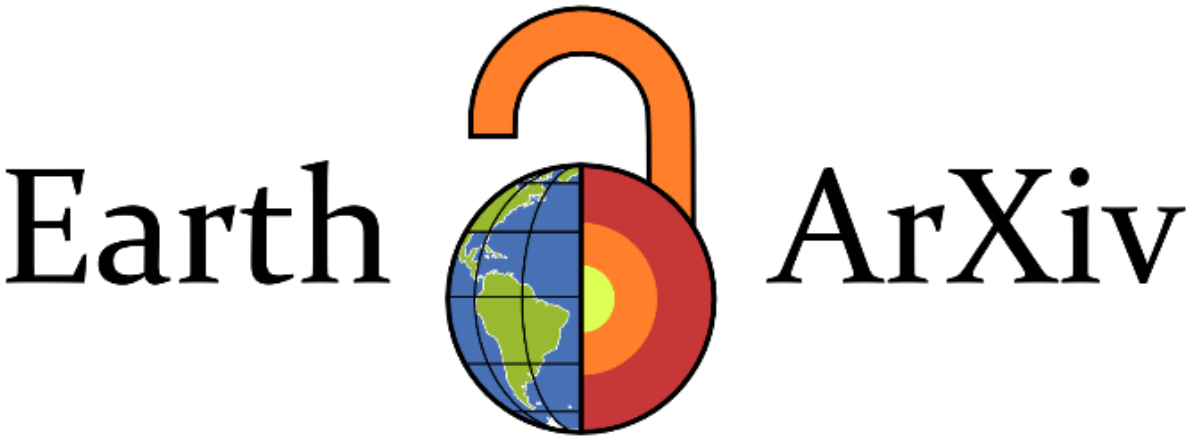

Smart Urban Design with Physics-Informed Neural Networks: Quantifying Temperature Reductions from Green Infrastructure Using Satellite Thermal Data

Dung Thi Vu[a], Rafeeque Ahmed Nizamani[b], Abdul Ghafoor Nizamani[c,1]

[a]*Istituto Nazionale di Geofisica e Vulcanologia, Sezione di Bologna, Viale Carlo Berti Pichat, 6/2, Bologna, 40127, BO, Italy*
[b]*School of Mechanical and Electronic Engineering, Wuhan University of Technology, Wuhan, Hubei, P.R. China*
[c]*Faculty of Computer Science, Engineering and Economics, Ostfold University College, BRA Veien 4, Halden, 1757, NO, Norway*

Abstract

Urban Heat Islands (UHIs), characterised by elevated temperatures in densely built environments, pose critical challenges to urban sustainability, public health, and energy resilience. Mitigating UHIs requires precise quantification of the cooling effects of green infrastructure; however, existing models often fail to integrate high-resolution geospatial data with physical laws. This study presents a novel Physics-Informed Neural Network (PINN) framework that addresses this gap by unifying satellite-derived data, including land surface temperature (LST), normalised difference vegetation index (NDVI), and emissivity, with vector-based urban features within a single predictive model. The framework innovatively embeds thermodynamic principles, such as heat diffusion equations, directly into the neural network's loss function, while a seamless GeoJSON (Geographic JavaScript Object Notation) to tensor format enables the integration of heterogeneous geospatial datasets. Applied to case studies in Bologna, Italy, and Washington, D.C., USA, the model accurately identified optimal locations for green infrastructure. A targeted intervention prioritising green roofs on buildings near railways in identified LST hotspots achieved a 99% reduction in the spatial extent of identified hotspots in Bologna and 98.7% in D.C., with an area-weighted average temperature decrease of 1.31°C and 1.30°C, and maximum localised cooling of 6.13°C and 8.48°C, respectively. A more comprehensive scenario incorporating green roofs near railways and new trees along main

*Corresponding: Abdul Ghafoor Nizamani (abdul.g.nizamani@hiof.no)

roads yielded even greater cooling, with hotspot reductions of 97.4% and 98.3%, and area-weighted average temperature drops of 1.51°C and 1.80°C for the two cities, respectively. Validation against Landsat 8 thermal imagery confirmed high predictive accuracy, with R^2 values of 0.926 and 0.937, demonstrating performance superior to conventional machine learning baselines. By bridging physics-constrained machine learning with geospatial analytics, this work provides a scalable, data-driven tool for smart urban design, offering actionable insights to combat UHIs through targeted, climate-adaptive planning.

Keywords: Deep learning, Physics-Informed Neural Networks, urban heat island mitigation, green infrastructure, land surface temperature.

---

1. Introduction

The Urban Heat Islands (UHIs) effect, a phenomenon whereby metropolitan areas experience significantly warmer temperatures than their rural surroundings, presents a mounting threat to sustainable urban development (Debbage& Shepherd, 2015; Nakata-Osaki et al., 2018). This thermal anomaly arises from multiple interconnected factors: i) anthropogenic heat emissions from vehicles and buildings; ii) extensive impervious surfaces with low albedo that absorb rather than reflect solar radiation; iii) reduced vegetation cover limiting evaporative cooling; and iv) urban geometry that traps heat through reduced wind flow and radiative trapping (Kim & Brown, 2021; Ming et al., 2024).

The consequences are severe and multifaceted. UHIs exacerbate heat-related mortality and morbidity, disproportionately affecting vulnerable groups such as the elderly and those with pre-existing health conditions (Ho et al., 2023; Cleland et al., 2023). They strain energy infrastructure by increasing cooling demand in some cases by over 120% (Li et al., 2019), while accelerating material degradation and disrupting local ecosystems (Lopes et al., 2025). In an era of accelerating global urbanisation and climate change, developing robust mitigation strategies has become paramount (Gartland, 2010; Eyni et al., 2025).

Two primary types of urban heat islands exist: surface urban heat islands (SUHIs) and atmospheric urban heat islands. SUHIs represent radiative temperature differences between impervious and natural surfaces, typically most intense during daylight hours, while atmospheric UHIs manifest as warmer urban air compared to surrounding rural areas, often most pronounced at night (Cui & De Foy, 2012; Wang et al., 2017). The intensity of SUHIs varies seasonally, typically reaching maximum values during summer months (Tian et al., 2021).

Quantifying this phenomenon relies heavily on satellite-derived Land Surface Temperature (LST) data from the thermal infrared spectrum (10–12 μm), which provides synoptic overviews of surface thermal patterns (Li et al., 2013). The urban heat island (UHI) intensity is quantified as $\Delta T_{u-r} = T_u - T_r$, where T_u represents urban temperature and T_r represents rural reference temperature (Yang & Liu, 2005; Venkatraman et al., 2024). Satellite remote sensing offers significant advantages for SUHIs monitoring, including continuous spatial coverage, global consistency, and simultaneous observation of multiple surface parameters (McCartney et al., 2020). However, limitations persist, including fixed acquisition times that may miss peak intensity periods, cloud cover obstruction, and atmospheric correction dependencies.

Among the most promising mitigation strategies is strategic implementation of green infrastructure (GI) including urban parks, green roofs, and permeable pavements, which counteracts urban heating through multiple biophysical mechanisms (Saaroni et al., 2018; Lin et al., 2025; Ching et al., 2025). Temperature reductions achieved through green infrastructure directly mitigate UHI effects through several pathways: i) evapotranspiration transforms sensible heat into latent heat, effectively cooling ambient air; ii) vegetation shading reduces solar radiation absorption by impervious surfaces; and iii) increased albedo reflects more incoming solar radiation (Zang et al., 2013; Cuce et al., 2025). Green roofs, comprising waterproof membranes, growing media, and vegetation layers over traditional roofs, provide additional thermal benefits through insulation that reduces heat flux into buildings (Arabi et al., 2015; Zipper et al., 2017). Critically, by lowering urban temperatures, green infrastructure reduces the ΔT_{u-r} differential that defines UHI intensity, thereby diminishing the heat island effect at its source.

However, a significant implementation gap persists between recognising GI's theoretical potential and deploying it efficiently. Urban planners often lack precise, scalable tools to answer critical questions: *Where would a new park deliver the greatest cooling benefit?* or *What quantifiable temperature reduction might a green roof policy achieve?*

Conventional approaches to understanding UHIs have typically relied on empirical studies or traditional machine learning models, such as Random Forests and Geographically Weighted Regression (Szymanowski & Kryza, 2011; Oukawa et al., 2022). These models establish statistical correlations between urban morphology and LST patterns . However, a growing body of literature highlights their fundamental limitations. A key critique is that while these data-driven models are useful for identifying statistical patterns, they often fail to respect the physical principles governing urban heat dynamics, such as diffusion and advection. As noted by Elbeltagi et al. (2025) and others, these models suffer from an empirical nature and a

'black box' framework, which hinders both interpretability and physical consistency (Khosravi et al., 2018; Kim et al., 2022). This lack of embedded physical laws means their predictions can be physically implausible. Furthermore, these models struggle with generalisability. A review by Mondal et al. (2024) confirms that machine learning approaches in urban energy modelling often perform poorly when applied to unseen urban morphologies or climatic regimes, as they are unable to reveal causal or physically-grounded relationships (Li & Wang, 2025). Consequently, their utility for scenario planning and proactive urban design is limited. They treat geospatial inputs as static predictors rather than dynamic components of a thermodynamic system (Ahmed et al., 2025). Ultimately, whilst AI-based models can accelerate predictions, they often fall short of the accuracy and physical fidelity offered by traditional numerical weather prediction or physics-based simulations (Yang et al., 2024). This underscores the value, as highlighted by Łach & Svyetlichnyy (2025), of embedding physical laws into predictive frameworks to ensure realism and transferability.

To address these shortcomings, a new paradigm has emerged: physics-informed machine learning. This framework seeks to integrate the predictive power of data driven models with the rigorous constraints of scientific principles. A leading example is the Physics-Informed Neural Networks (PINNs), designed to solve problems governed by partial differential equations (PDEs), such as the heat equation (Zhao et al., 2025) or the Navier-Stokes equations (Raissi et al., 2019; Bowman et al., 2023). The PINNs are trained not only to fit observational data but also to penalise solutions that violate the prescribed physical laws. This physics-based regularisation embeds prior knowledge directly into the model, ensuring that outputs are not just statistically sound but also thermodynamically consistent. This hybrid approach enhances model generalisation and reduces dependency on vast, perfectly labelled datasets, making it particularly suited for complex environmental systems where data may be sparse. Although PINNs have demonstrated considerable success in fields namely fluid mechanics (Eivazi et al., 2024; Botarelli et al., 2025), their application to the multi-scale, heterogeneous challenge of urban heat island modelling remains a novel and largely untapped area of research (Omrany & Al-Obaidi, 2024).

This study introduces a novel PINN framework designed to overcome the limitations of traditional models in urban climate analysis. Its primary contribution is the direct integration of high-resolution, vector-based geospatial data including GeoJSON building footprints (Butler et al., 2016), road networks, and the precise locations of GI with the governing equations of urban heat dynamics within a neural network architecture (Fig. 1). Unlike previous approaches that treat urban features as static predictors, our model dynamically incorporates them into a physics-constrained simulation of urban heat flows. This advance allows us not only to accurately reconstruct

existing LST patterns but also to conduct robust counterfactual analyses. We can therefore quantify the specific temperature reductions achievable through targeted GI interventions, such as installing green roofs or expanding urban parkland. We demonstrate the framework through case studies of Bologna, Italy, and Washington, D.C., USA. These cities chosen for their contrasting climates, urban morphologies, and patterns of heat vulnerability. Both face significant UHI challenges, where documented disparities in heat exposure often correlate with socioeconomic factors. After validating the model's performance against observed Landsat satellite data, we leverage its physics-informed foundation to map the potential cooling benefits of strategic green infrastructure deployment.

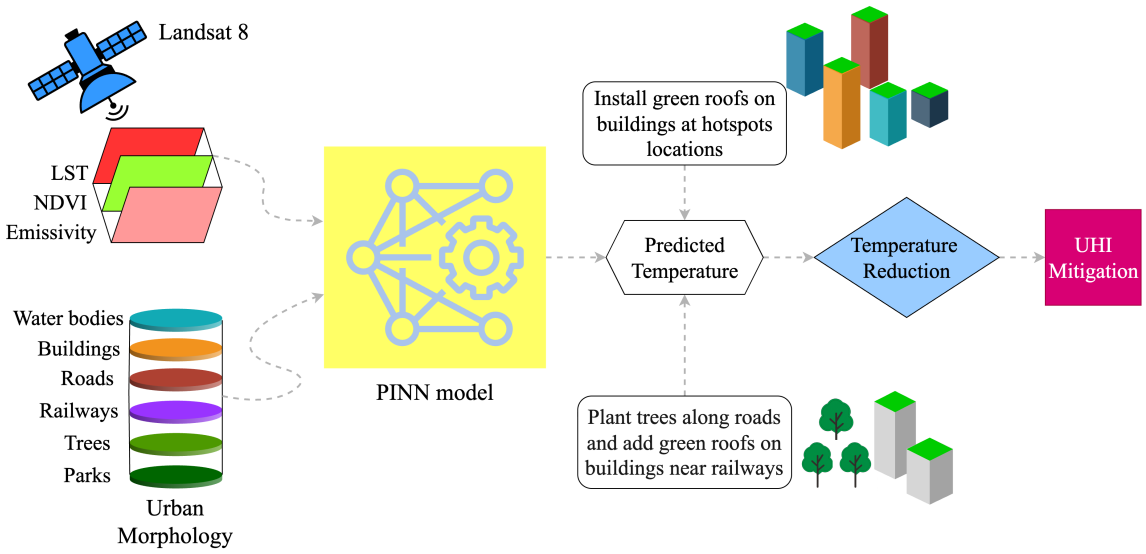

Figure 1: Schematic overview of the proposed Physics-Informed Neural Network (PINN) framework for quantifying green infrastructure cooling effects.

2. Methodology

This study employs PINNs to model urban land surface temperature. The model integrates satellite-derived inputs—LST, Normalised Difference Vegetation Index (NDVI), emissivity (EM), and urban morphological features to establish baseline thermal patterns. Once trained and validated, the PINNs predict ambient temperature reductions achievable through targeted green infrastructure interventions in high-heat zones.

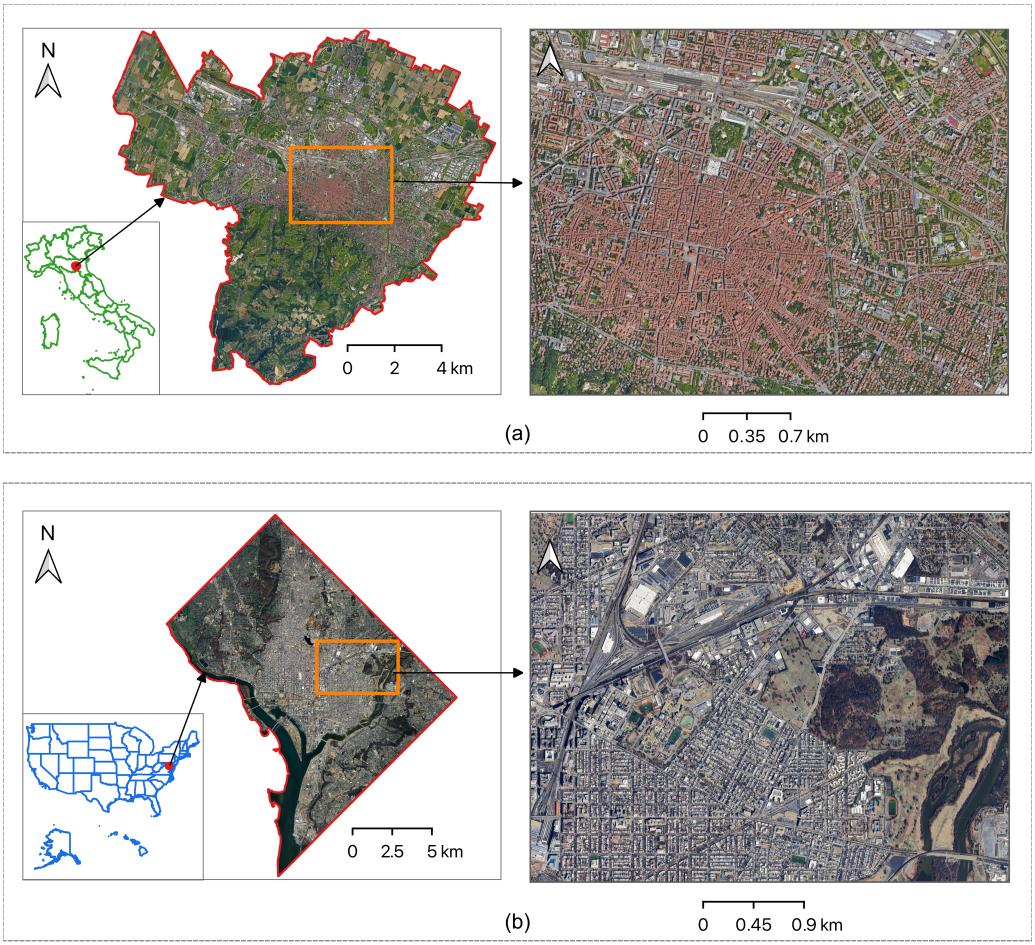

Fig. 2. Study areas: (a) Bologna, Italy, and (b) Washington D.C., USA.

2.1. Study Area and Data Acquisition

Our approach investigates two contrasting urban environments: Bologna, Italy (44.4949°N, 11.3426°E), and Washington D.C., USA (38.9072°N, 77.0369°W), as illustrated in Fig. 2. These cities were deliberately selected due to their divergent climatic zones—a Mediterranean influence in Bologna and a humid subtropical regime in D.C., alongside their unique urban morphologies and notable UHI intensities, which offer critical insights into the interplay between climate, city design, and thermal dynamics. The satellite-derived study areas (highlighted in orange) reflect distinct spatial patterns, with Bologna's compact historic core and D.C.'s grid-based expansion serving as focal points for comparative analysis. Cloud-free Landsat 8 observations (i.e., no NaN values) were acquired during summer periods when urban heat stress is most

severe, Bologna (15–31 July 2024) and Washington D.C. (15–30 June 2024).

Landsat 8 Collection 2 Level-2 surface reflectance and top-of-atmosphere (TOA) brightness temperature data were acquired via Google Earth Engine (Gorelick et al., 2017). LST, NDVI, and surface emissivity (EM) were prioritised as core PINN inputs due to their direct relevance to surface energy balance (SEB) components governing urban thermal dynamics. EM was selected over albedo because: i) it is essential for accurate LST retrieval; ii) it directly controls longwave radiation emission (a key nocturnal UHI driver); and iii) the Ermida et al. (2020) LST algorithm requires emissivity inputs. While albedo influences shortwave energy balance, its thermal effects are partially captured by NDVI (vegetation proxy), with EM being more critical for summer thermal dynamics.

LST represents the net radiative flux state variable, NDVI quantifies vegetation fraction (governing latent heat flux and albedo), and EM defines longwave radiation efficiency. These variables were computed using Ermida et al. (2020)'s single-channel method. Firstly, to calculate LST, the thermal infrared radiance (L_λ) from Band 10 was converted to at-sensor brightness temperature (T_B) via Planck's law:

$$T_B = \frac{K_2}{\ln\left(\frac{K_1}{L_\lambda} + 1\right)} \tag{1}$$

where $K_1 = 774.89$ W·m^{-2}·sr^{-1}·μm^{-1} scales radiance to temperature units, and $K_2 = 1321.08$ K corrects for sensor-specific thermal response offsets. Atmospheric correction employed the single-channel algorithm:

$$LST = \gamma \left[\frac{1}{\varepsilon}(\psi_1 L_\lambda + \psi_2) + \psi_3\right] + \delta + T_B \tag{2}$$

where ε denotes emissivity, γ and δ are Planck function parameters, and ψ_1, ψ_2, ψ_3 represent atmospheric functions of total precipitable water derived from NCEP/NCAR reanalysis (Kalnay et al., 2018). Output resolution is 30 m. Secondly, NDVI is derived from surface reflectance in near-infrared (ρ_{NIR}) and red (ρ_{red}) wavelengths (Bands 5 and 4):

$$NDVI = \frac{\rho_{NIR} - \rho_{red}}{\rho_{NIR} + \rho_{red}} \tag{3}$$

scaled to [-0.2, 0.3] using Collection 2 parameters. NDVI serves as a vegetation-mediated cooling proxy in the SEB equation. Thirdly, EM is critical for maintaining physical consistency in the heat diffusion equation. It is estimated via the NDVI

Thresholds Method (NDVITHM):

$$\varepsilon = \begin{cases} 0.99 & \text{water} \\ 0.989 & \text{snow/ice} \\ \varepsilon_v \cdot \text{FVC} + \varepsilon_s \cdot (1 - \text{FVC}) & \text{otherwise} \end{cases} \tag{4}$$

where $\varepsilon_v = 0.99$ (vegetation), ε_s is bare soil emissivity from ASTER GED, and Fractional Vegetation Cover (FVC) is derived as:

$$\text{FVC} = \left(\frac{\text{NDVI} - \text{NDVI}_{\text{soil}}}{\text{NDVI}_{\text{veg}} - \text{NDVI}_{\text{soil}}} \right)^2 \tag{5}$$

with $\text{NDVI}_{\text{soil}} = 0.2$ and $\text{NDVI}_{\text{veg}} = 0.86$.

Fig. 3 presents a comparative analysis of LST, NDVI, and emissivity for Bologna (a–f) and Washington D.C. (g–l) using Landsat 8 data. The spatial maps for Bologna (Fig. 3a–c) show moderate homogeneity across all three variables. The LST map (a) ranges from 33.8°C to 49.3°C, with dominant warm tones indicating widespread urban heat. The NDVI map (b) spans from –0.02 to 0.88, showing a mix of vegetated patches and built-up areas that suggest consistent vegetation cover. The emissivity map (c) ranges from 0.93 to 0.99, with most areas in the mid-to-high range (0.95–0.98), reflecting uniform surface materials like historic stone or concrete. The corresponding histograms (Fig. 3d–f) show sharply peaked distributions, indicating low variability for Bologna. The LST histogram (d) peaks narrowly around 41.5–45.4°C. The NDVI histogram (e) has a concentrated peak near 0.2–0.43, reflecting consistent vegetation density from features like small parks and tree-lined streets. The emissivity histogram (f) peaks sharply at 0.96–0.97, consistent with homogeneous building materials.

In contrast, Washington D.C.'s spatial maps (Fig. 3g–i) reveal greater heterogeneity. The LST map (g) spans 32.4°C to 52.9°C, with distinct cool and hot zones reflecting varied land use. The NDVI map (h) ranges from –0.36 to 0.91, showing pronounced green patches from large parks alongside extensive low-NDVI areas. The emissivity map (i) spans 0.95–0.99, with greater colour variation than Bologna's, including blue areas of low emissivity (e.g., from metal roofs or asphalt) and red zones of high emissivity (e.g., from vegetation or concrete). The histograms in D.C. (Fig. 3j–l) highlight broader, and multimodal distributions. The LST histogram (j) is wider, with peaks at both lower and higher temperatures. The NDVI histogram (k) shows a bimodal pattern, contrasting impervious surfaces with dense vegetation. The emissivity histogram (l) is also broader, with multiple sub-peaks reflecting varied materials.

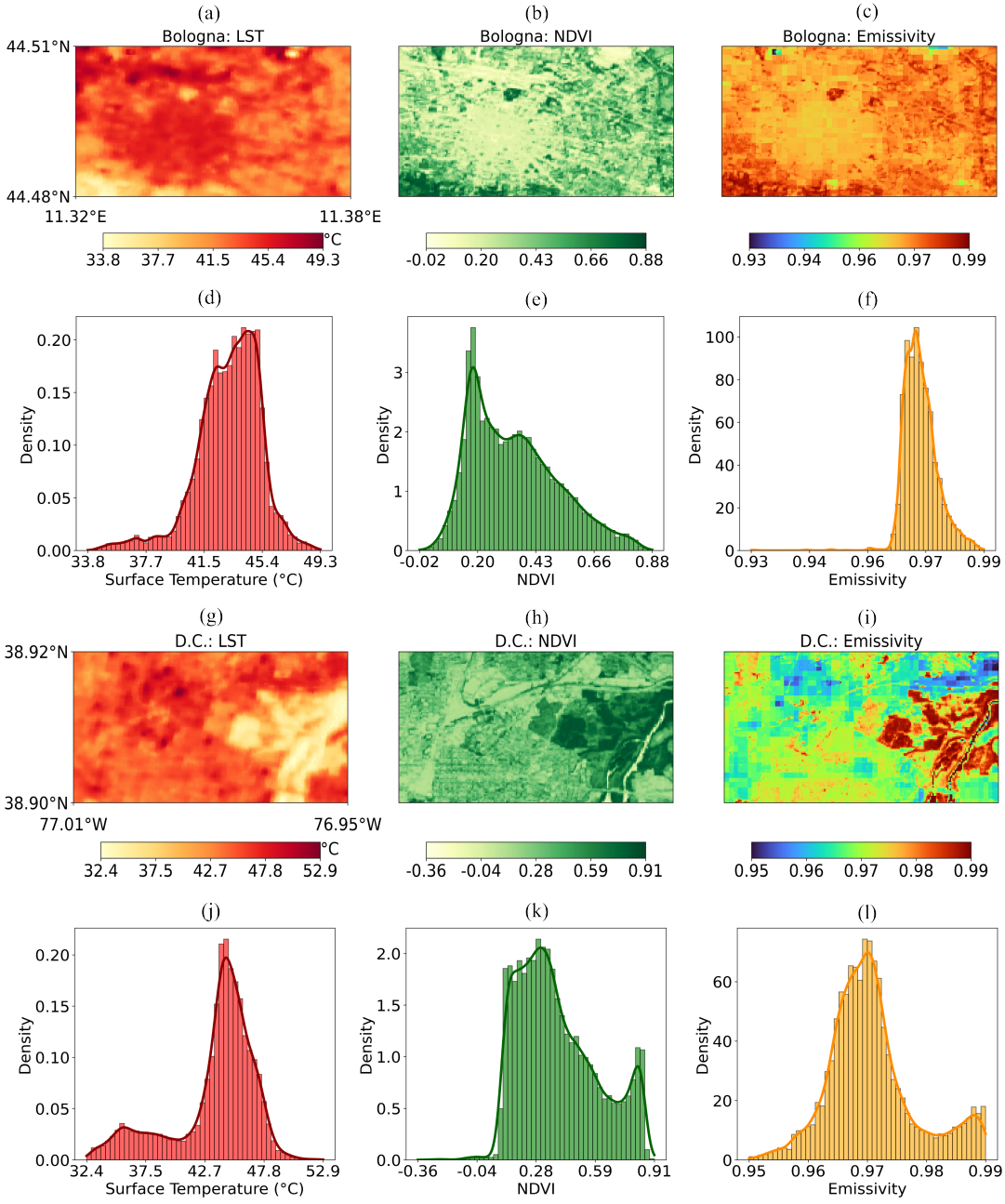

Fig. 3. Landsat 8-derived LST, NDVI, and emissivity maps for Bologna (a–c) and Washington D.C. (g–i), highlighting contrasting urban thermal patterns. Histograms emphasize sharper LST/NDVI peaks in Bologna (d–f) and broader distributions in D.C. (j–l), reflecting differences in urban density, vegetation cover, and surface materials.

Urban morphology elements were classified by thermal function: i) heat contributing features with impervious surfaces (buildings, roads, railways) correlate strongly with elevated LST due to high thermal admittance, low albedo, and limited evapotranspiration. These dominate UHI effects through radiative trapping and slow heat release; and ii) cooling features where parks (cumulative cooling via shading and soil moisture), dispersed trees (localised cooling through impervious surface shading), and water bodies (thermal inertia and evaporative cooling) explicitly model mitigation effects. This classification enables the PINNs to resolve heterogeneous impacts of urban components on thermal patterns.

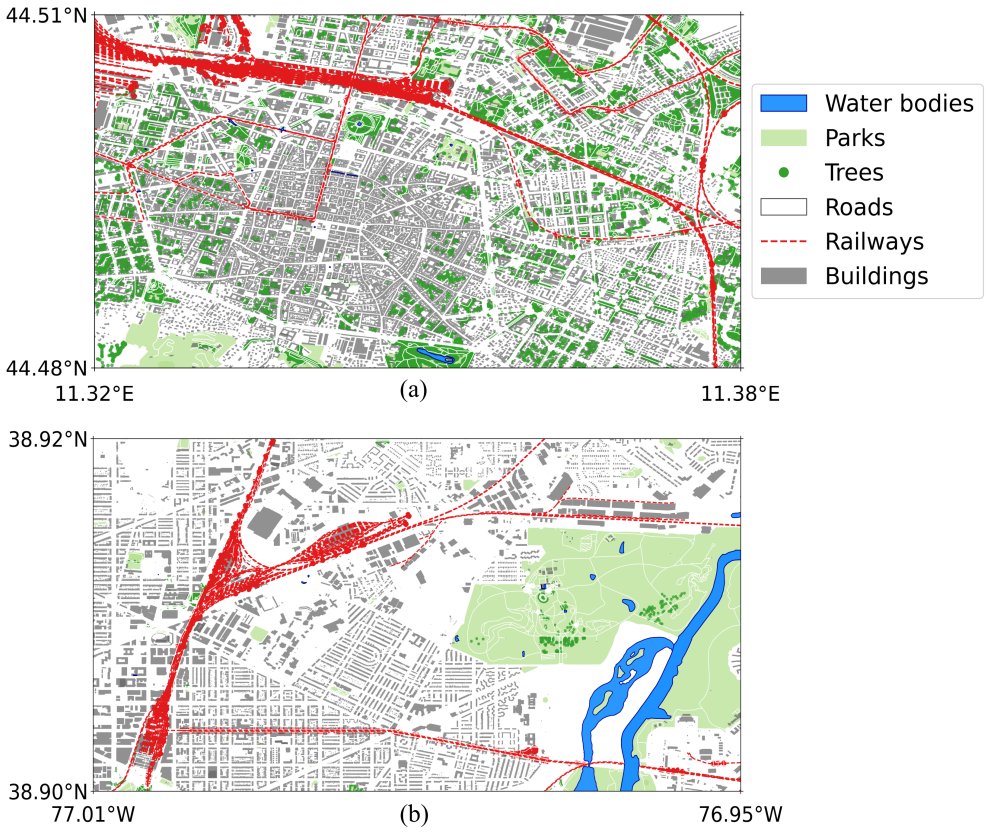

Fig. 4. Urban morphology of Bologna (a) and Washington D.C. (b), mapped with OSMnx data (Boeing, 2017). Key elements are water bodies (blue), parks (light green), trees (dark green dots), roads (white), railways (red lines), and buildings (gray rectangles).

Fig. 4 illustrates the contrasting urban morphologies of Bologna (a) and Washington D.C. (b), derived from OpenStreetMap data (Boeing, 2017). The maps reveal

distinct planning paradigms shaped by their history. Bologna exhibits a high-density, medieval layout with a fine-grained mix of buildings (gray polygons), roads (white lines), and railways (red lines). Green spaces (i.e., parks with light green and trees with dark green dots) and water bodies (blue) are sparse and integrated within the dense urban fabric. On the other hand, Washington D.C. displays a planned, hierarchical structure with more segregated land use. Large parks and the Potomac River define its edges, while a radial road network and a prominent railway separate zones. These morphological differences (i.e., Bologna's compact, integrated form versus D.C.'s dispersed, and segregated one), directly influence each city's environmental sustainability, mobility, and heat retention, as explored through the thermal function classification.

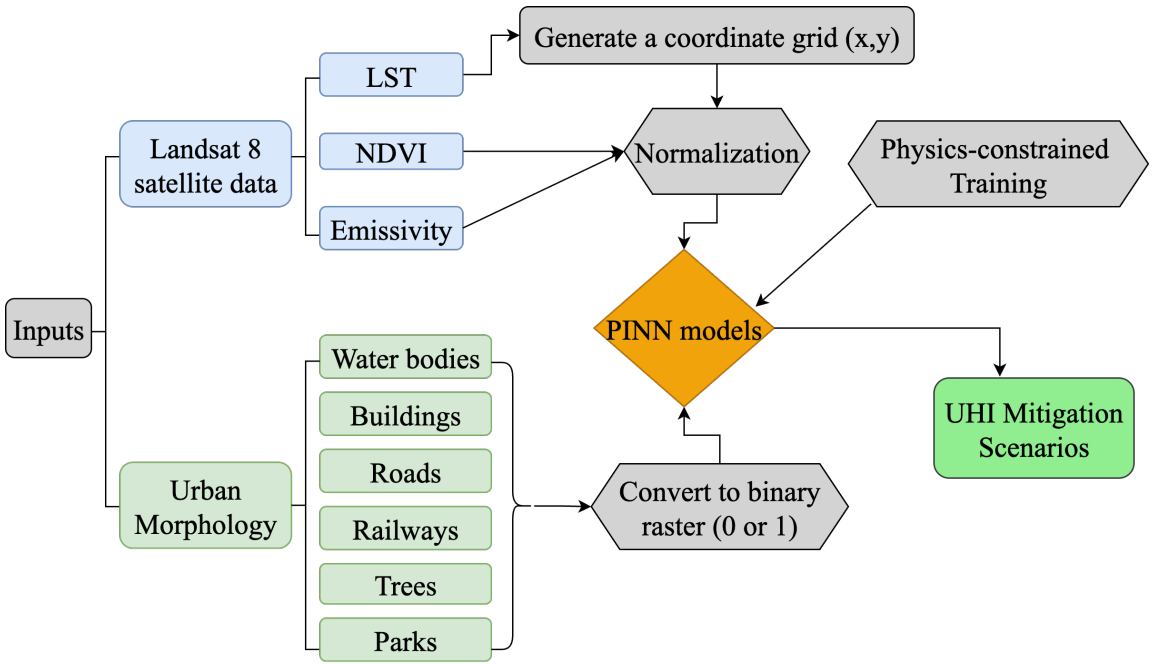

Fig. 5. Preprocessing workflow for Landsat 8 and urban morphology data into PINN models, generating UHI mitigation scenarios via physics-constrained training with standardized coordinates.

2.2. Data Preprocessing

The preprocessing pipeline employed a three-stage approach to ensure spatial coherence, feature compatibility, and numerical stability for PINN modelling (Fig. 5).

Stage 1: Geometric Alignment. All raster datasets (LST, NDVI, and emissivity) were reprojected to the appropriate Universal Transverse Mercator (UTM) coordinate system for each study area. This used zone 32N for Bologna and zone 18N for Washington D.C., employing bilinear resampling. This enforced a consistent 30-metre resolution, congruent grids, and pixel-perfect spatial registration via affine transformations from raster metadata.

Stage 2: Urban Feature Rasterisation. Vector GeoJSON data for urban features (buildings, roads, railways, parks, water bodies, trees) were converted into binary rasters. Using spatial point-in-polygon operations, each 30m pixel was assigned a value of 1 (feature present) or 0 (absent), creating layers that precisely matched the Landsat raster extents.

Stage 3: Input Standardisation. All input variables were min-max normalized to a [0,1] range. This prevented scale dominance, accelerated neural network convergence, ensured numerical stability, and maintained dimensional consistency for physics-based loss terms. The final 10-channel input tensor integrated normalized spatial coordinates, NDVI, emissivity, and the six binary urban feature rasters.

2.3. Physics-Informed Neural Network Architecture

The PINN architecture developed in this study models the urban heat island effect by solving a material-dependent heat diffusion equation, integrating data-driven learning with physical governing laws (Cai et al., 2021). The core framework employs a multi-branch fully connected network that processes normalised input features, consisting spatial coordinates, NDVI, emissivity, and six urban feature channels, through sequential transformation layers (Fig. 6).

The architecture facilitates stable computation of higher-order derivatives essential for the physics-informed loss component. Initial processing layers use Tanh activations for smooth feature extraction, while middle layers incorporate LeakyReLU activations (negative slope = 0.01) to mitigate vanishing gradients and enhance information flow during backpropagation (Bowman et al., 2023).

2.3.1. Thermal Diffusivity Parameterisation

The physical constraint is implemented through the steady-state heat equation adapted for heterogeneous urban environments (Chen et al., 2022; Xing et al., 2023):

$$\nabla \cdot \left(k(\mathbf{x}) \nabla \widehat{\mathrm{T}}(\mathbf{x}) \right) = \mathrm{Q}(\mathbf{x}) \quad \text{in } \Omega, \tag{6}$$

which expands to:

$$\nabla k(\mathbf{x}) \cdot \nabla \widehat{\mathrm{T}}(\mathbf{x}) + k(\mathbf{x}) \nabla^2 \widehat{\mathrm{T}}(\mathbf{x}) = \mathrm{Q}(\mathbf{x}). \tag{7}$$

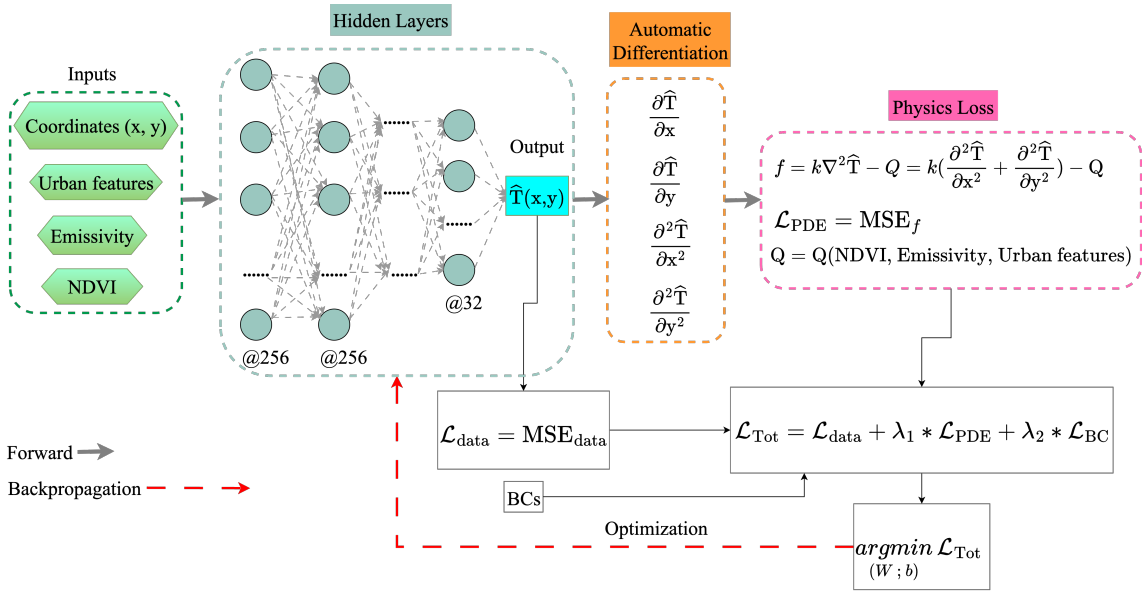

Fig. 6. PINN architecture for urban thermal modeling. The network enforces the heat equation $k\nabla^2\widehat{\mathrm{T}} = \mathrm{Q}$ through automatic differentiation, where k (thermal diffusivity) and Q (heat sources) are computed from urban features (buildings, vegetation, water). Boundary conditions (BCs) apply Dirichlet constraints (fixed temperature) at urban edges and Neumann constraints (zero flux) at water/park boundaries. Loss weights ($\lambda_1 = 0.1, \lambda_2 = 0.3$ for Bologna; $\lambda_2 = 0.5$ for D.C.) reflect city-specific morphological constraints.

Urban environments comprise diverse materials (concrete, asphalt, vegetation, water) with distinct thermal properties. Our model computes pixel-specific k values from material composition, enabling appropriate penalisation of heat equation violations: rapid diffusion through dense urban materials (high k) versus slow diffusion through vegetated or aqueous areas (low k).

For computational efficiency and numerical stability, we use a simplified form of the heat equation:

$$k(\mathbf{x})\nabla^2\widehat{\mathrm{T}}(\mathbf{x}) = \mathrm{Q}(\mathbf{x}). \tag{8}$$

This formulation assumes that the spatial gradient of thermal diffusivity, ∇k, is sufficiently small that the term $\nabla k \cdot \nabla \mathrm{T}$ can be considered secondary to the dominant diffusion behaviour (Xing et al., 2023). This approximation is reasonable given: i) the relatively smooth spatial variation of material properties at our resolution scale; ii) the primary focus on capturing bulk diffusion characteristics rather than sharp interfacial fluxes; and iii) numerical stability considerations in the PINN frameworks.

Thermal diffusivity values are assigned based on land cover. For discrete land cover types:

$$k = \begin{cases} k_{\text{water}} = 0.19 & \text{if water} > 0.5 \\ k_{\text{veg}} = 0.33 & \text{if parks} \cup \text{trees} > 0.5 \\ k_{\text{urban}} = 1.0 & \text{otherwise} \end{cases} \tag{9}$$

For mixed pixels, k is calculated as a weighted average:

$$k_{\text{mixed}} = \frac{(\text{urban\_weight} \times k_{\text{urban}}) + (\text{veg\_weight} \times k_{\text{veg}}) + (\text{water\_weight} \times k_{\text{water}})}{\text{total\_weight}} \tag{10}$$

where weights derive from normalised urban feature inputs with buildings, roads, rails for urban (urban_weight); parks, trees for vegetation (veg_weight); water for water bodies (water_weight). Absolute thermal diffusivity values (water: 0.14×10^{-6} m^2/s, vegetation: 0.25×10^{-6} m^2/s, urban: 0.75×10^{-6} m^2/s) were normalised relative to urban areas.

2.3.2. Heat Source/Sink Term

The term Q represents distributed heat sources (Q > 0) or sinks (Q < 0), parameterizing key urban processes beyond simple diffusion. The formulation synthesizes established relationships from urban climate literature, where anthropogenic heat and land cover are frequently decomposed into constituent proxies (Lu et al., 2024; Chen et al., 2022; Wang et al., 2023). The structure of Q is defined as:

$$\begin{aligned} \text{Q} \quad &= \alpha_1 \times (1 - \text{NDVI}) + \alpha_2 \times (1 - \text{emissivity}) + \alpha_3 \times \text{buildings} + \alpha_4 \times \text{roads} \\ &\quad + \alpha_5 \times \text{railways} + \alpha_6 \times \text{parks} + \alpha_7 \times \text{water} + \alpha_8 \times \text{trees} \end{aligned} \tag{11}$$

The signs and relative magnitudes of the coefficients are set as physically informed priors based on domain knowledge (Table 1). For instance, the stronger cooling coefficient for trees ($\alpha_8 = -0.25$) compared to parks ($\alpha_6 = -0.2$) reflects the enhanced shading and transpiration of dense canopy cover (Wang et al., 2023), while the positive coefficients for impervious surfaces align with models of anthropogenic heat flux (Lu et al., 2024). The use of (1−emissivity) is supported by its established role in urban surface energy balance, where lower emissivity materials increase heat retention (Siddiqui et al., 2025). Within the PINN frameworks, these priors guide the model to learn causal relationships consistent with physical principles rather than merely spatial patterns. The specific coefficient values are initial estimates, and their precise magnitudes can be calibrated or learned from data, ensuring the model remains adaptable while being structurally constrained for physically plausible predictions, especially in data-sparse regions (Chen et al., 2022).

Table 1: Coefficients and their physical interpretation for the term Q.

Feature	**Coefficient**	**Physical Interpretation**
NDVI	$\alpha_1 = +0.2$	Reduced vegetation (low NDVI) increases heat
Emissivity	$\alpha_2 = +0.05$	Lower emissivity increases heat retention
Buildings	$\alpha_3 = +0.15$	Anthropogenic heat/wall geometry effects
Roads	$\alpha_4 = +0.08$	Asphalt heat absorption
Railways	$\alpha_5 = +0.05$	Railway heat absorption (metal/concrete)
Parks	$\alpha_6 = -0.2$	Shading and transpiration cooling
Water bodies	$\alpha_7 = -0.2$	Evaporative cooling and high heat capacity
Trees	$\alpha_8 = -0.25$	Enhanced shading and transpiration cooling

2.3.3. Boundary Conditions and City-Specific Configuration

The system is constrained by hybrid boundary conditions applied at the domain perimeter $\partial\Omega$, defined as the outermost 5-pixel perimeter of the raster grid. This approach separates the physical modelling of the interior urban landscape from the prescribed behaviour at its edges. Firstly, Dirichlet condition (fixed temperature) on urban boundaries ($\partial\Omega_D$):

$$\widehat{\mathrm{T}}(\mathbf{x}) = \mathrm{T}_{\text{observed}}(\mathbf{x}) \quad \text{on } \partial\Omega_D, \tag{12}$$

where $\mathrm{T}_{\text{observed}}$ is the satellite-measured temperature. This anchors the model to physical reality for anthropogenic surfaces (buildings, roads, rails), whose temperatures are strongly governed by local properties and are less influenced by external, non-urban areas. Secondly, Neumann condition (zero flux) on natural boundaries ($\partial\Omega_N$):

$$\frac{\partial\widehat{\mathrm{T}}(\mathbf{x})}{\partial n} = 0 \quad \text{on } \partial\Omega_N, \tag{13}$$

where $\partial\widehat{\mathrm{T}}/\partial n$ is the derivative normal to the boundary. This represents an insulating condition for natural features (parks, water), preventing unrealistic heat exchange outside the domain. It reflects that the temperatures of these features are governed by internal processes like evapotranspiration and thermal inertia, rather than by the abstracted "outside" of the modelled domain.

City-specific architectural configurations (Table 2) address distinct urban morphologies. Bologna's compact fabric uses dual LeakyReLU layers and lower boundary

weighting ($\lambda_2 = 0.3$) to capture complex intra-urban variations with relaxed perimeter constraints. Washington D.C.'s sprawling layout employs a single LeakyReLU followed by Tanh activation and higher boundary weighting ($\lambda_2 = 0.5$) to enforce constraints along extensive natural boundaries while modelling broader thermal gradients.

2.4. Loss Functions

The training objective minimizes the composite loss function ($\mathcal{L}_{\text{Tot}}$) introduced in Eq. 14, which combines data fidelity, physical consistency, and boundary constraints:

$$\mathcal{L}_{\text{Tot}} = \mathcal{L}_{\text{data}} + \lambda_1 \mathcal{L}_{\text{PDE}} + \lambda_2 \mathcal{L}_{\text{BC}} \tag{14}$$

The data loss computes the mean squared error between predictions and observations for interior pixels:

$$\mathcal{L}_{\text{data}} = \frac{1}{N_I} \sum_{i \in \text{Interior}} \left(\widehat{\text{T}}_{\text{pred}}(x_i, y_i) - \text{T}_{\text{obs}}(x_i, y_i) \right)^2 \tag{15}$$

The physics loss enforces the modified heat equation (Eq. 8) throughout the domain:

$$\mathcal{L}_{\text{PDE}} = \frac{1}{N_I} \sum_{i \in \text{Interior}} \left(k(x_i, y_i) \cdot \nabla^2 \widehat{\text{T}}_{\text{pred}}(x_i, y_i) - \text{Q}(x_i, y_i) \right)^2 \tag{16}$$

The boundary loss implements the hybrid conditions defined in Eqs. 12 and 13, where λ_N is a small, fixed weight equal 0.1 for the Neumann term.:

$$\mathcal{L}_{\text{BC}} = \mathcal{L}_{\text{Dirichlet}} + \lambda_N \mathcal{L}_{\text{Neumann}} \tag{17}$$

with:

$$\mathcal{L}_{\text{Dirichlet}} = \frac{1}{N_D} \sum_{i \in \partial\Omega_{\text{Urban}}} \left(\widehat{\text{T}}_{\text{pred}}(x_i, y_i) - \text{T}_{\text{obs}}(x_i, y_i) \right)^2 \tag{18}$$

$$\mathcal{L}_{\text{Neumann}} = \frac{1}{N_N} \sum_{i \in \partial\Omega_{\text{Natural}}} \left\| \frac{\partial \widehat{\text{T}}_{\text{pred}}}{\partial n}(x_i, y_i) \right\|_2^2 \tag{19}$$

All spatial derivatives, including the Laplacian $\nabla^2 \widehat{\text{T}}$ and normal derivative $\partial \widehat{\text{T}} / \partial n$, are computed via automatic differentiation. The city-specific weighting strategy for λ_1 and λ_2 follows the morphological considerations detailed in Section 2.3 and Table 2.

Table 2: Unified PINN Architecture and City-Specific Hyperparameters

Component	**Configuration**
Architecture	**Shared Structure:** Input: 10 Neurons (x, y, NDVI, Emissivity, 6 urban features) Input Block: Linear(256) → Tanh(); Linear(256) → Tanh() Physics Block: Linear(128) → Tanh(); Linear(64) → Tanh() Output: Linear(32) → Tanh(); Linear(1) **Middle Block (City-Specific):** - Bologna: Linear(256) → LeakyReLU; Linear(128) → LeakyReLU - Washington D.C.: Linear(256) → LeakyReLU; Linear(128) → Tanh
Hyperparameters	**Shared:** Physics Loss Weight (λ_1): 0.1 Optimizer: Adam (LR=0.001) Batch Size: 512; Epochs: 300 **City-Specific:** - Boundary Loss Weight (λ_2): 0.3 (Bologna), 0.5 (Washington D.C.)
Total Parameters	194,177

2.5. Training Procedure

The training protocol was consistent across both city models to ensure that performance differences stemmed solely from the tailored architectural and hyperparameter configurations rather than optimization variations.

We employed the Adam optimizer (Kingma & Ba, 2014) with an initial learning rate of 0.001 to navigate the complex loss landscape of the PINNs (194,177 parameters). A ReduceLROnPlateau (Thakur et al., 2024) scheduler monitored validation loss, reducing the learning rate by a factor of 10 after 5 epochs without improvement. This approach prevented oscillatory behavior and enabled finer convergence.

Training used a batch size of 512 for stable gradient updates and ran for 300 epochs to sufficient for convergence of both data fidelity and physics constraints.

The comparative training trajectories (Fig. 7) reveal how urban morphology fundamentally shapes model convergence. Bologna exhibited higher initial total loss (≈ 0.08) compared to Washington D.C. (≈ 0.04), reflecting the greater thermal complexity of its dense, organic urban fabric. Both models showed rapid initial data loss reduction, but Bologna's slower asymptotic convergence (stabilizing at ≈ 0.005 after 200 epochs versus D.C.'s ≈ 0.002) indicates persistent challenges in capturing fine-scale thermal heterogeneity. To confirm the robustness of our final model selections, we conducted a comprehensive hyperparameter sensitivity analysis, detailed in Supplementary Appendix A.

2.6. Model Evaluation

The PINN model's performance was rigorously evaluated through quantitative metrics and spatial diagnostics applied independently to each urban case study. This comprehensive assessment framework validated predictive accuracy and spatial fidelity at the 30 m pixel scale.

Three key metrics quantified pixel-level predictive accuracy. The Coefficient of Determination (R^2) measured the proportion of variance explained by the model:

$$R^2 = 1 - \frac{\sum_{i=1}^{n}(T_i - \widehat{T}_i)^2}{\sum_{i=1}^{n}(T_i - \overline{T})^2} \tag{20}$$

where n denotes the total number of pixels (Bologna: $n = 21,614$; Washington D.C.: $n = 24,200$), T_i represents observed LST, $\widehat{T}_i$ predicted LST, and $\overline{T}$ the mean observed LST.

The Root Mean Square Error (RMSE) expressed average prediction error in degrees Celsius:

$$\mathrm{RMSE} = \sqrt{\frac{1}{n}\sum_{i=1}^{n}(T_i - \widehat{T}_i)^2} \tag{21}$$

The Mean Absolute Error (MAE) provided a robust interpretation of error magnitude:

$$\mathrm{MAE} = \frac{1}{n}\sum_{i=1}^{n}|T_i - \widehat{T}_i| \tag{22}$$

Spatial diagnostics complemented these metrics through visualization of absolute errors:

$$E_{\mathrm{abs},i} = |\widehat{T}_i - T_i| \tag{23}$$

Error heatmaps employed a diverging coolwarm colourmap (blue: errors <1°C; red: errors >3°C), masked to urban cores to highlight discrepancies in high-density zones. This approach facilitated identification of systematic errors associated with specific urban morphologies and infrastructure configurations.

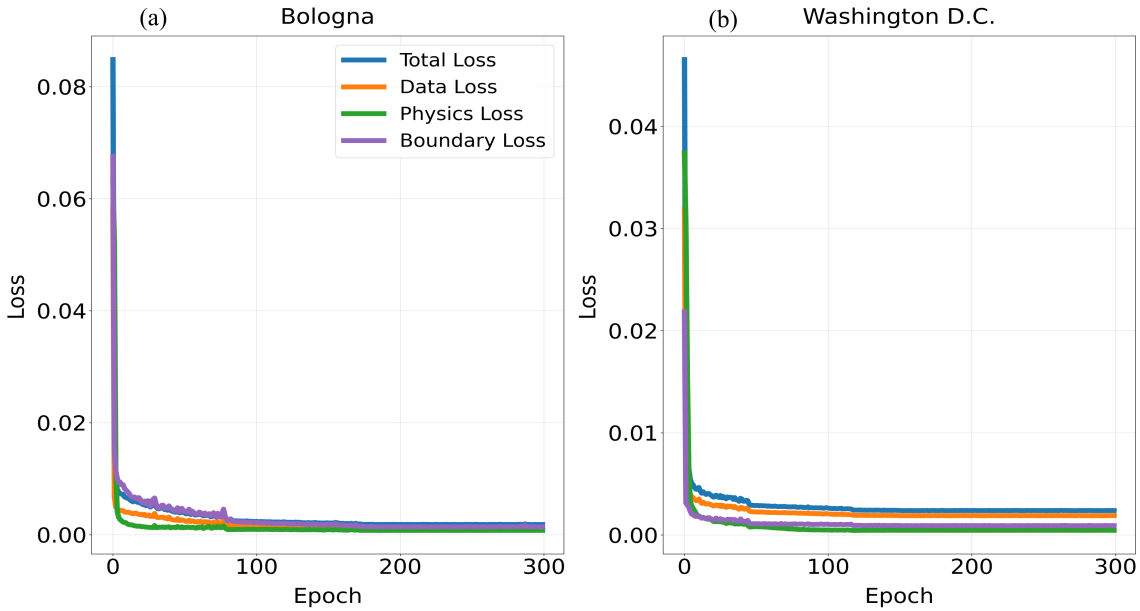

Fig. 7. Comparative training history of PINN for Bologna (a) and Washington D.C. (b), showing evolution of total loss (blue), data loss (orange), physics loss (green), and boundary loss (pink) across 300 epochs.

3. Results

This section validates the PINN framework's predictive accuracy and demonstrates its utility for urban heat mitigation planning. We first assess the model's performance in reconstructing observed Landsat 8 LST patterns (Subsection 3.1), then evaluate two targeted intervention scenarios: i) green roof deployment in UHI hotspots identified by LST and the Urban Heatwave Thermal Index (UHTI) (Nardino et al., 2022) (Subsection 3.2), and ii) an integrated strategy combining tree planting along roads with green roofs near railways (Subsection 3.3).

3.1. Validation of PINN-Predicted Land Surface Temperature

The PINN models demonstrate strong performance in reconstructing land surface temperature patterns across both urban environments. Quantitative comparison

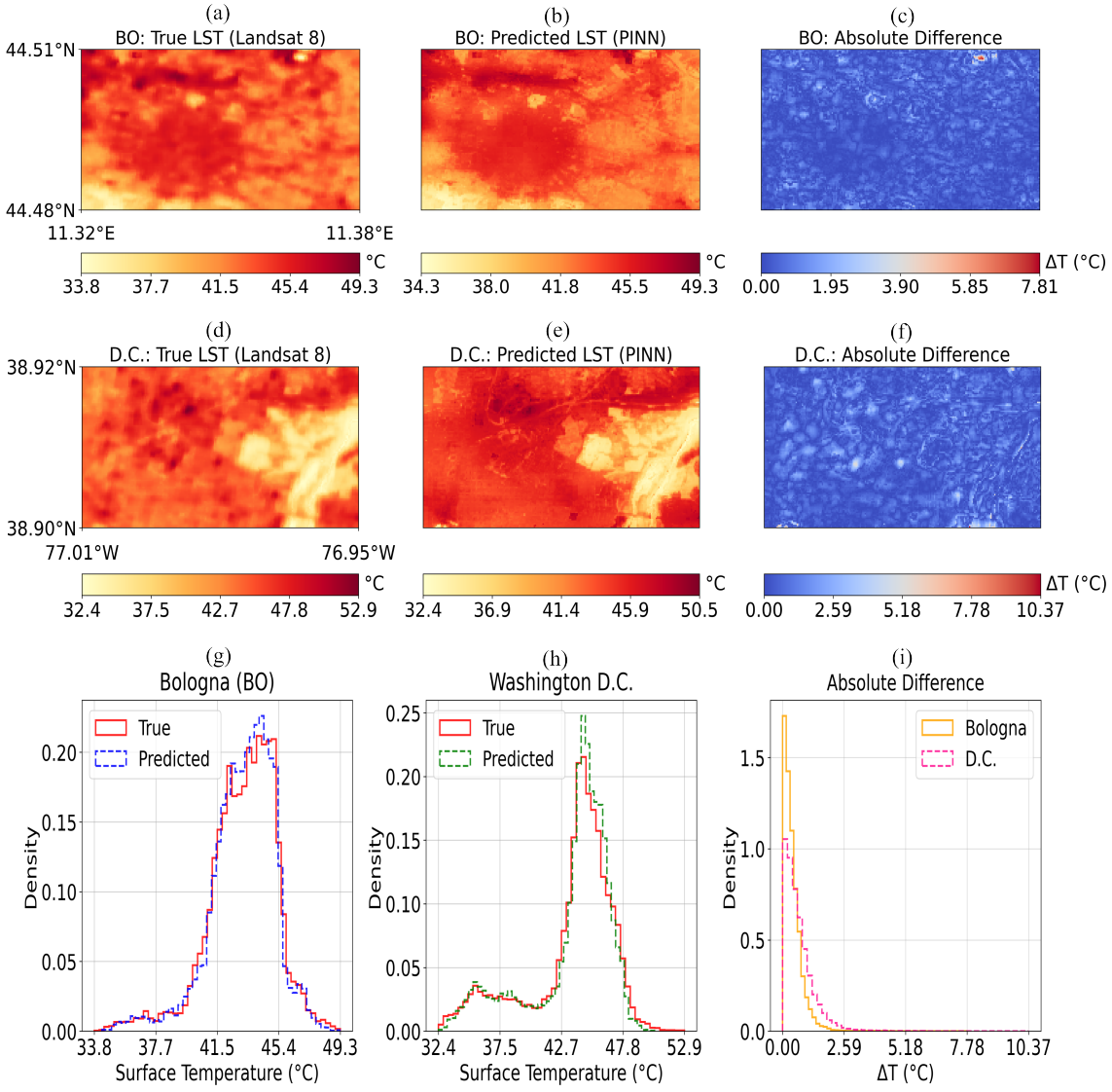

Fig. 8. Spatial and statistical comparison of Landsat 8 true LST (a, d) and PINN-predicted LST (b, e) with absolute errors (c, f) for Bologna (a–c) and Washington D.C. (d–f). Density plots (j, h) show strong alignment between true (red) and predicted (blue/green) LST distributions, while error density (i) confirms tight clustering near 0°C for both cities, with Bologna exhibiting marginally lower errors.

between predicted and observed LST reveals high accuracy, with spatial distributions and statistical metrics confirming the model's capability to capture urban heat island

dynamics.

Fig. 8 compares true Landsat 8 LST (left) with PINN-predicted LST (center) and their absolute differences (right) for Bologna and Washington D.C. Spatially, Bologna's true LST (a; 33.8–49.3°C) and predicted LST (b; 34.3–49.3°C) show strong visual correspondence, with absolute errors (Fig. 8c) predominantly ≤3.9°C (blue-dominated), peaking near 0°C.

For D.C., true LST (Fig. 8d; 32.4–52.9°C) and predictions (e; 32.4–50.5°C) also align well, though absolute differences (Fig. 8f) reach up to 10.37°C, with larger errors in specific regions (e.g., water bodies). Statistically, density plots (Fig. 8j, h) confirm tight overlap between true (red) and predicted (blue/green) LST distributions for both cities, with peaks in the 41–45°C range for Bologna and broader clustering for D.C. The absolute difference density (Fig. 8i) reveals Bologna's errors are more tightly clustered near 0°C (orange) compared to D.C. (pink), indicating higher prediction precision for Bologna due to its tighter error distribution (e.g., 90% of errors <2°C), whereas D.C.'s broader error spread (up to 10.37°C) stems from heterogeneous land cover (e.g., water bodies, fragmented vegetation), which increases local uncertainty despite a strong overall model fit. This spatial and statistical alignment demonstrates the PINN model's ability to replicate observed thermal patterns while highlighting how urban complexity influences error distribution.

Despite these differences, both cities achieve very high coefficients of determination ($R^2 > 0.92$), confirming the model's robust performance across diverse urban landscapes. The complete performance metrics (Table 3) show Bologna achieving lower error metrics (RMSE = 0.58°C, MAE = 0.42°C) compared to Washington D.C. (RMSE = 0.92°C, MAE = 0.67°C), reflecting the greater complexity of D.C.'s heterogeneous urban fabric.

Table 3: Performance metrics

City	R^2	RMSE (°C)	MAE (°C)
Bologna	0.9260	0.5781	0.4153
Washington D.C.	0.9370	0.9160	0.6724

3.2. Cooling Potential of Green Roofs in Urban Heat Island Hotspots

3.2.1. Introduction and Intervention Framework

UHIs pose significant challenges in densely built environments, exacerbating thermal stress and energy consumption. To address this, green roofs (GRs)—a nature-based solution—offer promise in mitigating UHI effects, specifically GRs applied in Bologna (Cipolla et al., 2017) and Washington D.C. (Ghaffari, 2021). The cooling

potential of green roofs stems from two primary biophysical processes: evapotranspiration, where plants and substrate release moisture, transforming sensible heat into latent heat and thereby cooling the ambient air, and enhanced albedo, where the vegetated surface reflects more solar radiation compared to conventional dark roofs (Mihalakakou et al., 2023). Furthermore, the layer of growing media and vegetation provides thermal insulation, reducing heat flux into buildings and mitigating the heat storage characteristic of urban materials (Sánchez-Cordero et al., 2025).

This subsection evaluates the cooling potential of strategically installing green roofs in identified UHI hotspots using the systematic approach outlined in Fig. 9. We applied the Urban Heat Thermal Index (UHTI) (Nardino et al., 2022) to pinpoint critical areas:

$$\mathrm{UHTI} = \mathrm{LST} \times (1 - \mathrm{NDVI}) \times (1/\varepsilon_{\mathrm{safe}}) \tag{24}$$

where $\varepsilon_{\mathrm{safe}} = \max(\varepsilon, 0.01)$ ensures numerical stability.

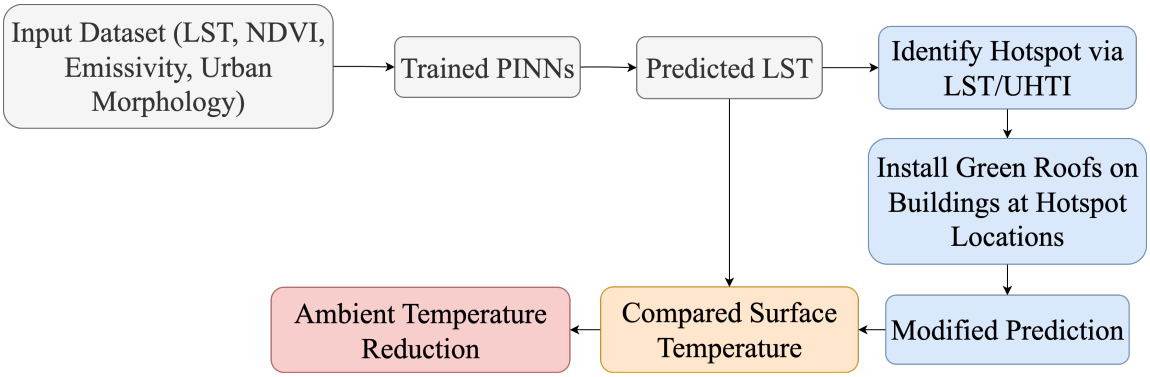

Fig. 9. Workflow for assessing green roof cooling potential in urban heat island hotspots.

3.2.2. Thermal Hotspot Classification

Hotspots were classified into six categories using percentile thresholds applied to both LST and UHTI distributions (Fig. 10). Cool spots (classes 1–3) used the 5th, 10th, and 15th percentiles, while hot-spots (classes 4–6) used the 85th, 90th, and 95th percentiles.

Table 4 quantifies the thermal thresholds for both cities. Bologna's LST-based hot spots range from 45.14°C to 46.07°C, while Washington D.C. exhibits more extreme thresholds (46.63°C to 47.73°C), reflecting its hotter summer climate. The UHTI thresholds further highlight these climatic differences, with D.C. showing higher values across all hotspot categories. Spatially, Bologna displays scattered hot spots

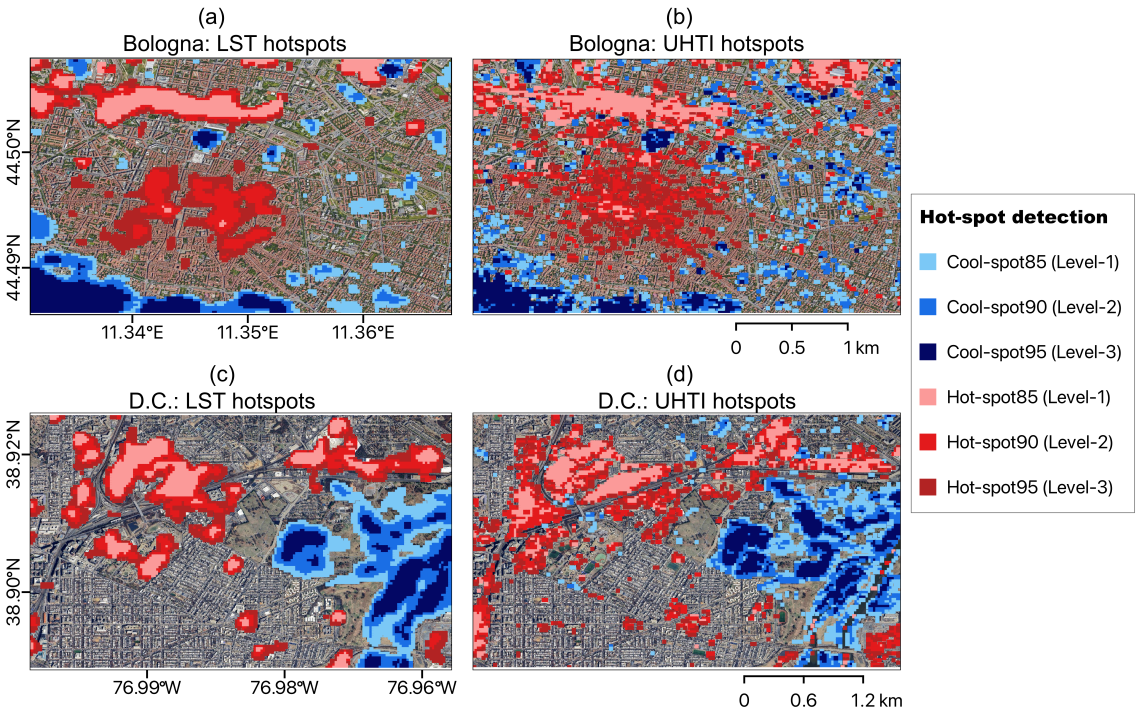

Fig. 10. Comparative analysis of LST- and UHTI-based hot/cool spot distributions in Bologna (a–b) and Washington D.C. (c–d), revealing distinct thermal patterns influenced by urban structure and climatic contexts.

interspersed with cooler urban patches, while its UHTI map reveals broader areas of heat retention in built-up zones. Washington D.C.'s LST map features a prominent cool zone (the Potomac River) surrounded by intense urban heat cores, with UHTI revealing more fragmented cool spots due to variable vegetation cover. The divergence between LST and UHTI thresholds underscores UHTI's sensitivity to contextual factors beyond temperature alone, providing a more nuanced identification of heat-vulnerable areas for targeted intervention.

3.2.3. Green Roof Implementation Methodology

We evaluated green roof cooling potential across four strategic deployment scenarios: i) non-rail buildings in LST hotspots, ii) non-rail buildings in UHTI hotspots, iii) rail-adjacent buildings in LST hotspots, and iv) rail-adjacent buildings in UHTI hotspots. Building proximity to railways was defined using geospatial buffering with a 15-pixel radius, classifying intersecting buildings as "near-rail" for separate anal-

Table 4: Thermal hotspot classification thresholds

Threshold Level	Percentile	Bologna		Washington D.C.	
		LST (°C)	UHTI (°C)	LST (°C)	UHTI (°C)
Cool Level 1	5th	39.59	13.58	35.39	6.72
Cool Level 2	10th	40.71	17.32	37.04	9.74
Cool Level 3	15th	41.30	19.79	38.98	13.99
Hot Level 1	85th	45.14	38.41	46.63	39.37
Hot Level 2	90th	45.44	39.15	47.13	40.99
Hot Level 3	95th	46.07	40.72	47.73	42.76

ysis. For each scenario, NDVI and emissivity values were extracted from building rooftops and refined using Interquartile Range (IQR) filtering to ensure robust analysis. Green roofs were parameterized with $\mathrm{NDVI}_{\mathrm{GRs}} = 0.65$, a conservative value reflecting the practical reality of extensive green roofs with shallow growth media and hardy vegetation. Emissivity was dynamically computed using established vegetation fraction models Hulley et al. (2015):

$$P_v = \frac{\mathrm{NDVI}_{\mathrm{GRs}} - \mathrm{NDVI}_{\mathrm{soil}}}{\mathrm{NDVI}_{\mathrm{veg}} - \mathrm{NDVI}_{\mathrm{soil}}}, \qquad \varepsilon_{\mathrm{GRs}} = \varepsilon_v \cdot P_v + \varepsilon_s \cdot (1 - P_v) \tag{25}$$

with $\mathrm{NDVI}_{\mathrm{soil}} = 0.2$, $\mathrm{NDVI}_{\mathrm{veg}} = 0.5$, $\varepsilon_v = 0.985$, and $\varepsilon_s = 0.96$.

3.2.4. LST-Based Targeting Strategy

Fig. 11 presents a data-led strategy for deploying green roofs, targeting thermal hotspots (red points) in Bologna and Washington D.C., distinguishing between buildings away from railways (a, c) and those adjacent to them (b, d). The targeted buildings exhibited characteristically low vegetation cover, with median NDVI values of 0.18 (Bologna) and 0.16 (D.C.) for non-rail hotspots, and even lower values of 0.14 (Bologna) and 0.13 (D.C.) in rail-adjacent zones (provided in Supplementary Appendix Table A2). The proposed green roof sites (yellow rectangles) are concentrated within dense clusters of hotspots, particularly near railways where greenery is scarce.

The cooling efficacy analysis reveals distinct patterns across deployment scenarios. Fig. 12 presents PINNs-modeled LST comparisons with and without green roofs for non-rail hotspots in Bologna and Washington D.C. (associated with locations of green roofs at Fig. 11a,c). For Bologna (a–f), baseline LST (a) spans 34.3–49.6°C,

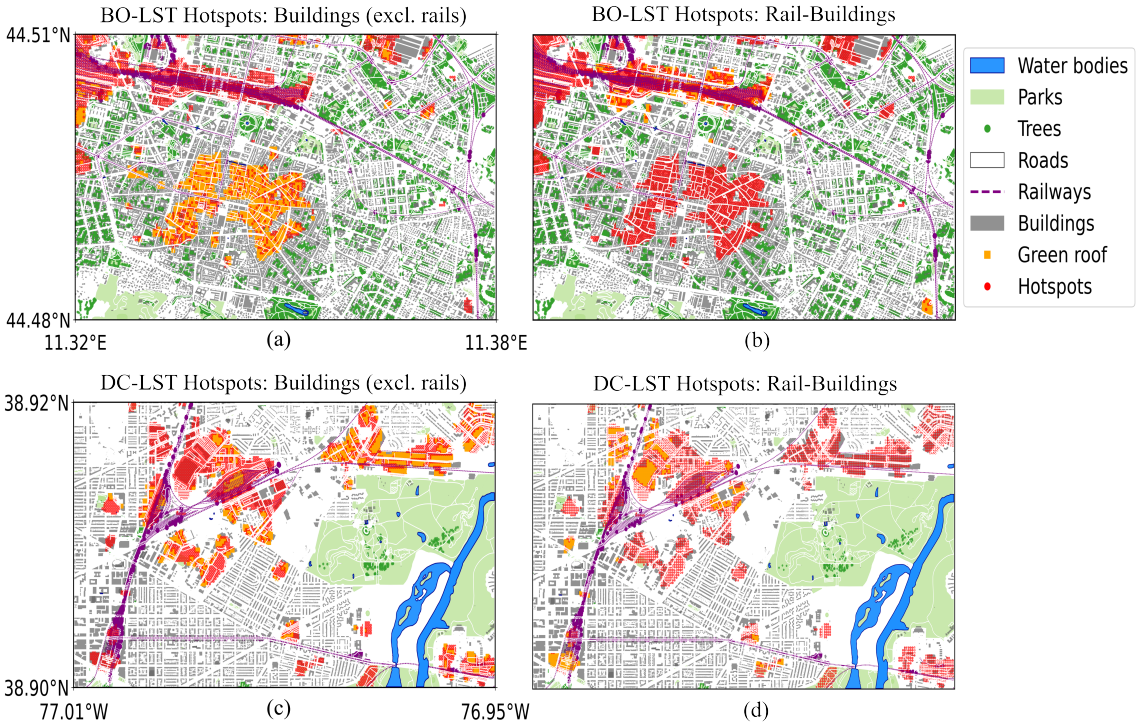

Fig. 11. Strategic green roof placement (yellow rectangles) in LST-detected hotspots (red points), targeting non-rail urban buildings (a,c) and buildings near railways (b,d) in Bologna and D.C.

with 72.0% of pixels concentrated in the 41.9–45.8°C range (d). Green roof implementation (b) shifts the distribution toward cooler temperatures, reducing the peak bin to 71.0% (e) while increasing the 38.1–41.9°C bin from 19.7% to 21.2%. Temperature reduction analysis (c, f) shows 96.1% of pixels unchanged ($\Delta T = 0$°C), while 4.0% exhibit cooling up to −6.13°C, clustered near −1.53°C. In Washington D.C. Fig. 12(g–l), baseline LST (g) ranges 32.4–50.5°C, with 57.8% of pixels in 41.4–45.9°C (j). Green roofs (h) induce a more pronounced leftward histogram shift (k), decreasing the peak bin to 50.7% and increasing cooler pixel proportions. The temperature reduction map (i) reveals significant cooling (up to −8.48°C) in linear hotspot corridors targeted by green roofs (Fig. 11c). This enhanced cooling reflects the cumulative effect of green roofs applied to areas with pre-existing solar panel infrastructure in D.C.'s urban fabric. Temperature reduction analysis (Fig. 12i, l) shows 97.5% of pixels unchanged, but the 2.5% of cooled pixels achieve greater maximum cooling compared to Bologna, with higher density reductions between −2.12°C and −8.48°C.

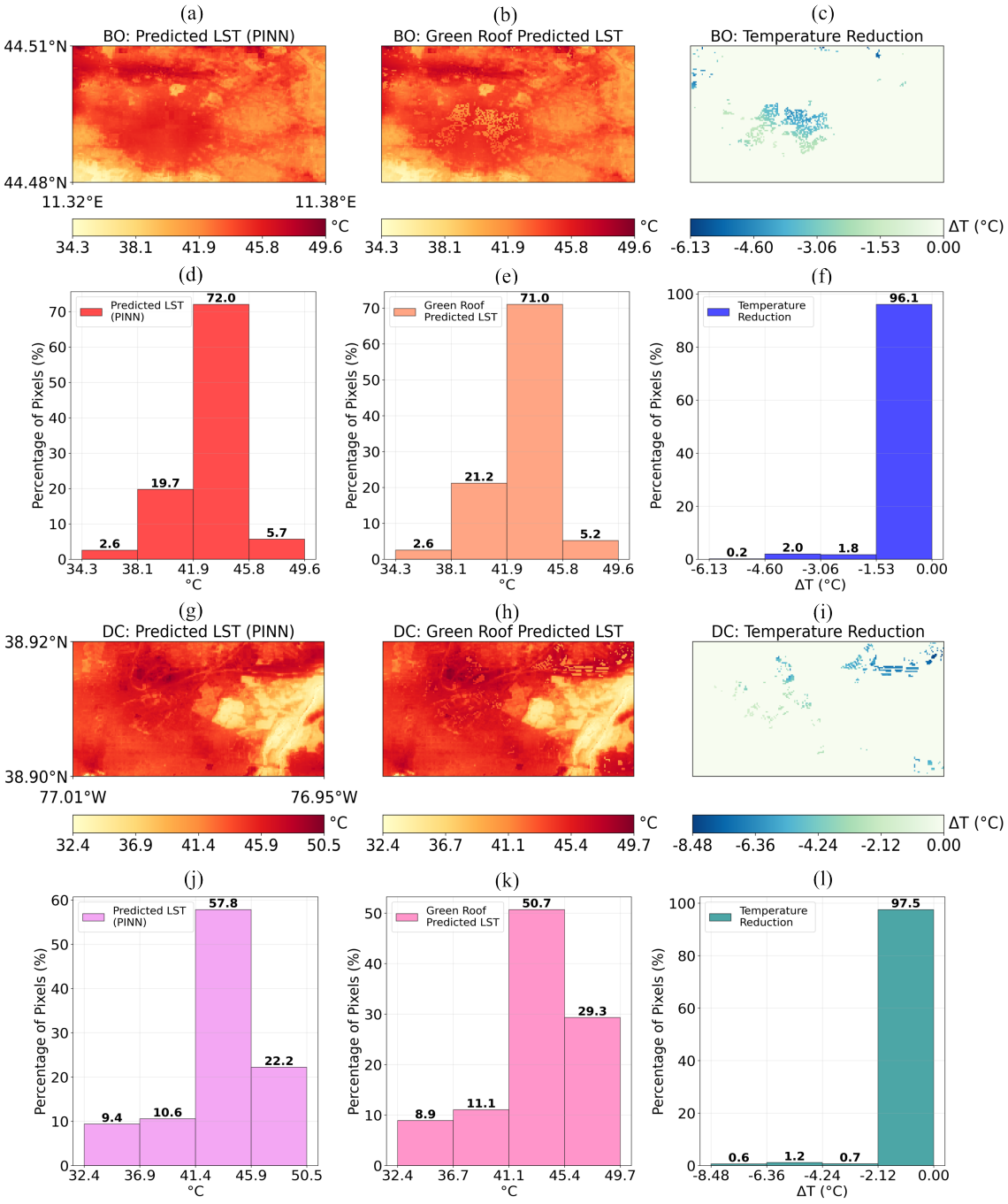

Fig. 12. PINNs-modeled LST comparison (with/without green roofs) and temperature reduction in non-rail LST hotspots for Bologna (a-f) and D.C.(g-l). D.C. shows stronger localized cooling (−8.48°C max) than Bologna (−6.13°C max) due to urban morphology differences.

For rail-adjacent with LST hotspots (Fig. 13), the cooling patterns diverged significantly between cities (aligned with locations of green roofs at Fig. 11b,d). In Bologna, baseline LST (a; 34.3–49.6°C) and green roof scenarios (b) show minimal visual change, with temperature reductions (c) concentrated in narrow corridors (max $\Delta T = -5.22$°C). Violin plots (d–e) quantify this minimal impact: baseline LST (d) shows 72.0% of pixels at 41.9–45.8°C, while green roofs (e) slightly increase cooler pixels (38.1–41.9°C from 19.7% to 20.0%) with nearly identical median temperature (41.9°C). Temperature reduction distribution (f) is heavily skewed toward 0°C (99.0% no change), confirming green roofs only impact localized rail-corridor hotspots.

Washington D.C. exhibits more pronounced changes, with baseline LST (g; 32.4–50.5°C) and green roof LST (Fig. 13h) showing clearer spatial differences. Temperature reduction patterns (Fig. 13i) highlight fragmented cooling, while violin plots (Fig. 13j–k) reveal a stronger distribution shift. The temperature reduction distribution (Fig. 13l) shows 98.7% of pixels unchanged but more significant cooling outliers (down to −5.21°C) compared to Bologna. This contrast stems from differences in rail corridor integration: Bologna's uniform urban fabric limits heat retention in rail zones, while D.C.'s fragmented corridors intersect hotter, less vegetated areas where green roofs more effectively mitigate concentrated thermal stress. This analysis demonstrates that green roof effectiveness hinges on existing layout, with varied cities like D.C. seeing the most cooling.

3.2.5. UHTI-Based Targeting Strategy

Fig. 14 shows the proposed deployment of green roofs (yellow) within Urban Heat Thermal Index (UHTI) hotspots in Bologna and Washington, D.C., contrasting sites away from railways (subplots a, c) with those inclusive of railway-adjacent areas (subplots b, d). The corresponding NDVI values for these areas (provided in Supplementary Appendix Table A3) show median values of 0.16 for non-rail buildings in Bologna and 0.13 in Washington, D.C. For buildings near railways, the median NDVI is lower, at 0.13 and 0.12 respectively. Unlike Fig. 11, which targets LST-detected hotspots (red points) representing current surface heat intensity, UHTI in Fig. 14 adopts a broader vulnerability framework. This framework explicitly expands targeting to rail - adjacent areas, recognizing infrastructure proximity as a key factor in heat vulnerability. In Fig. 11, green roofs are confined to discrete LST hotspots (e.g., scattered red zones in Fig. 11a/c for non - rail areas and concentrated rail - proximate hotspots in Fig. 11b/d). In contrast, Fig. 14 shows more extensive green roof deployment in rail - inclusive zones (b, d), where UHTI classifies larger contiguous areas near railways as heat vulnerable even if these areas do not exhibit

the highest LST values. For instance, in Bologna's rail - inclusive subplot (Fig. 14b vs. Fig. 11b), UHTI identifies a wider zone of vulnerability along rail corridors, leading to more widespread green roof placement compared to the narrower LST - based targeting in Fig. 11.

Similarly, in D.C. (Fig. 14d vs. Fig. 11d), UHTI's rail - inclusive approach captures additional vulnerable areas near railways that LST alone would overlook. This comparison underscores a critical methodological shift: Fig. 11 is reactive, addressing existing thermal hotspots, while Fig. 14 is proactive, using UHTI to prioritize potential vulnerability in rail - adjacent zones, reflecting a strategic expansion of green infrastructure to mitigate heat risks before they manifest as extreme LST values (aligned with thermal hotspot classification at Table 4).

Fig. 15 shows the temperature reduction (ΔT) achieved by green roofs in the UHTI-identified hotspots from Fig. 14, with results presented separately for non-rail (top) and rail-adjacent buildings (bottom) in Bologna (BO) and Washington, D.C. (DC). Contextualised by the data in Tables 5 and 6, the analysis reveals key differences in cooling effectiveness between the UHTI-driven targeting method and approaches based solely on LST, as shown in Fig. 12 and 13.

In non-rail UHTI hotspots (Fig. 15a–f), green roofs alter the thermal profiles. Bologna's Predicted LST (a) has 72.6% of pixels in the hottest range (41.9–45.8°C; Table 5), while the green roof predicted LST (b) reduces this to 70.6%, with 2.3% of pixels experiencing a cooling between -3.32°C and -1.66°C. Similarly, in DC (d), the proportion of pixels in the 41.4–45.9°C range drops from 57.8% to 50.6% with green roofs, and 0.6% of pixels achieve a maximum cooling of -8.48°C, a strong localised effect confirmed in Fig. 12i. These results are consistent with the LST-only targeting for non-rail hotspots in Fig. 12, where both cities show similar shifts in LST ranges and comparable maximum ΔT values (e.g., -6.13°C vs. -6.64°C for Bologna). This parity, validated in Tables 5 and 6, indicates that the UHTI framework, which incorporates vulnerability factors like rail proximity, retains the efficacy of LST-only targeting in non-rail areas.

For rail-adjacent UHTI hotspots (Fig. 15g–l), the improvement over the LST-only method (Fig. 13) is pronounced. In Bologna's rail-buildings (Table 5), 72.0% of pixels remain in the 41.9–45.8°C range for the Green Roof predicted LST, but 0.3% now achieve a cooling of -4.96°C. This is significantly better than the minimal median ΔT observed near zero in Fig. 13f. Washington, D.C. shows the same trend, with 0.5% of pixels reaching -5.21°C cooling, far exceeding the minimal mitigation in Fig. 13. This divergence is quantified in Tables 5 and 6, which show that UHTI targeting shifts 0.3% (BO) and 0.7% (DC) of pixels into the -2.48°C to -1.24°C cooling range, whereas the LST-only approach shows negligible cooling beyond -1.3°C.

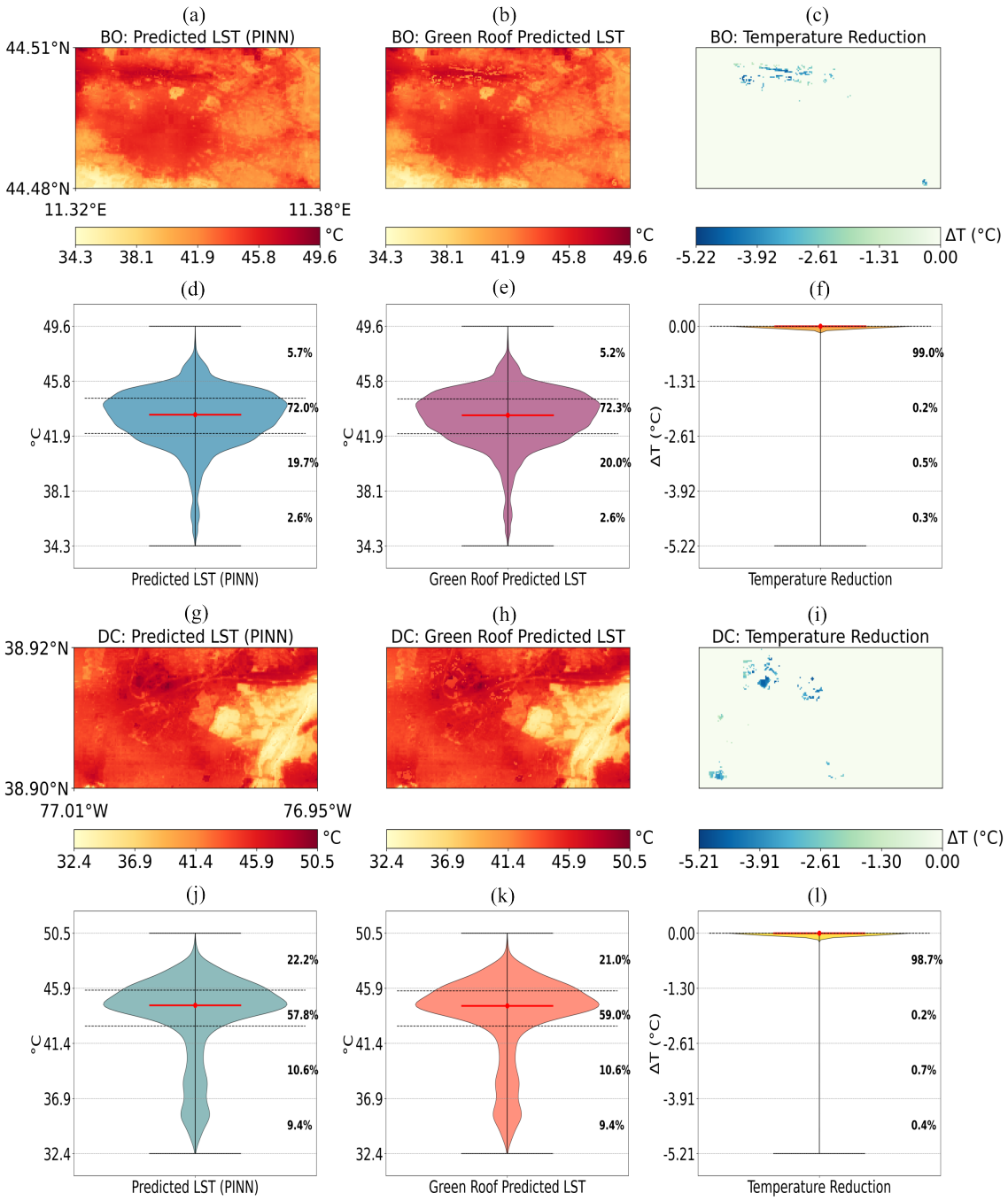

Fig. 13. Comparison of predicted LST (using PINN) and green roof intervention LST, alongside temperature reduction analyses for rail-adjacent LST hotspots in Bologna (a-f) and D.C. (g-l).

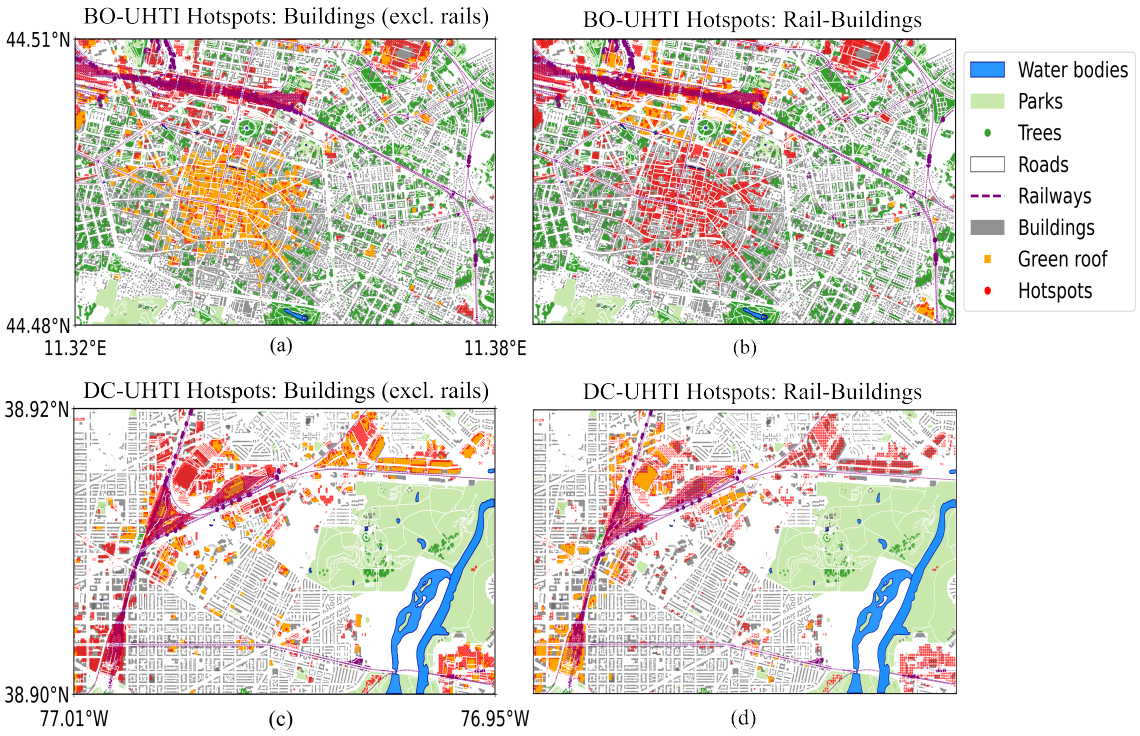

Fig. 14. Green roofs (yellow square) deployed in UHTI hotspots: non-rail buildings (a, c) and rail-inclusive zones (b, d) for Bologna (BO) and Washington D.C. (DC), reflecting UHTI's expanded targeting of rail-adjacent heat-vulnerable areas.

The key finding is that UHTI's vulnerability framework successfully extends targeting to rail-adjacent zones without reducing efficacy in non-rail areas. While the cooling achieved in non-rail areas is similar for both UHTI and LST-only methods, UHTI's rail-inclusive strategy enables meaningful thermal mitigation in zones where LST-only methods fail. For example, Bologna's UHTI rail-buildings (Fig. 15i) display clustered cooling patterns (blue zones) that are absent in the LST-only results (Fig. 13a–f). This contrast highlights UHTI's dual advantage: it maintains the precision of LST-driven methods in high-heat areas while proactively addressing vulnerability near railways, as evidenced by the higher proportion of pixels experiencing significant cooling. Overall, UHTI bridges the gap between reactive LST-based mitigation and the limitations of rail-adjacent LST targeting, offering a more comprehensive strategy for urban heat resilience.

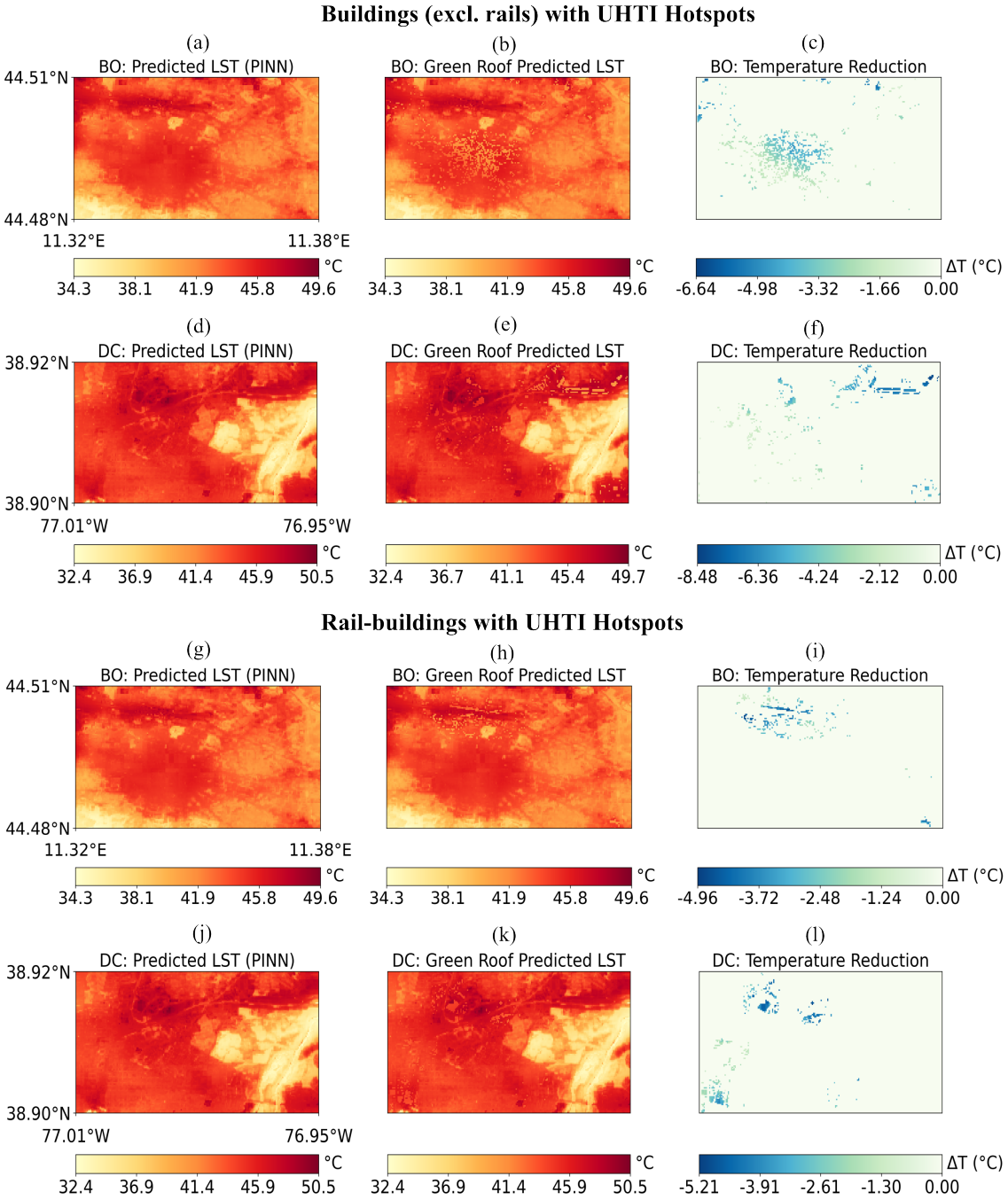

Fig. 15. UHTI hotspot-driven green roof impact in non-rail buildings (excl. rails): LST predictions and temperature reductions for Bologna (a–c) and D.C. (d–f); and rail-buildings with UHTI hotspots: LST predictions and temperature reductions for Bologna (g–i) and D.C. (j–l).

Table 5: Bologna with UHTI Hotspots Analysis

Scenario	Range 1	Range 2	Range 3	Range 4
Buildings (excl.rails)	34.3–38.1°C 2.6%	38.1–41.9°C 19.7%	41.9–45.8°C 72.0%	45.8–49.6°C 5.7%
	Predicted LST (PINN)			
	34.3–38.1°C 2.6%	38.1–41.9°C 21.7%	41.9–45.8°C 70.6%	45.8–49.6°C 5.2%
	Green roof Predicted LST			
	-6.64 to -4.98 °C 0.1%	-4.98 to -3.32°C 1.7%	-3.32 to -1.66°C 2.3%	-1.66 to 0°C 95.9%
	Temperature reduction			
Buildings near rails	34.3–38.1°C 2.6%	38.1–41.9°C 20.3%	41.9–45.8°C 72.0%	45.8–49.6°C 5.2%
	Green roof Predicted LST			
	-4.96 to -3.72°C 0.3%	-3.72 to -2.48°C 0.8%	-2.48 to -1.24°C 0.3%	-1.24 to 0°C 98.5%
	Temperature reduction			

3.3. Integrated Urban Greening Strategy: Trees and Green Roofs

This subsection evaluates an integrated greening strategy combining tree planting along main roads with green roof installations on rail-adjacent buildings. The approach targets high-heat zones where thermal stress is most acute and populations may be disproportionately vulnerable (Baqa et al., 2025).

The strategy leverages complementary biophysical processes: trees provide shading and evapotranspiration cooling (Knight et al., 2021), while green roofs reduce temperatures through enhanced evapotranspiration, albedo, and thermal insulation (Mihalakakou et al., 2023). The combined interventions were evaluated using our PINN frameworks (Fig. 16).

3.3.1. Integrated Intervention Methodology

To identify suitable green roof locations, buildings in close proximity to railways were selected using a 50-metre spatial buffer around the railway lines. Those intersecting this zone were classified as 'near-rail'. We then applied an NDVI threshold (≤ 0.2) to isolate structures lacking vegetation, followed by interquartile range filtering to exclude statistical outliers. This methodology identified 905 priority buildings

Table 6: D.C. with UHTI Hotspots Analysis

Scenario	Range 1	Range 2	Range 3	Range 4
Buildings (excl.rails)	32.4-36.9°C 9.4%	36.9-41.4°C 10.6%	41.4-45.9°C 57.8%	45.9-50.5°C 22.2%
	Predicted LST (PINN)			
	32.4-36.7°C 8.9%	36.7-41.1°C 10.9%	41.1-45.4°C 50.6%	45.4-49.7°C 29.6%
	Green roof Predicted LST			
	-8.48 to -6.36°C 0.6%	-6.36 to -4.24°C 1.0%	-4.24 to -2.12°C 0.6%	-2.12 to 0°C 97.8%
	Temperature reduction			
Buildings near rails	32.4-36.9°C 9.4%	36.9-41.4°C 10.6%	41.4-45.9°C 59.3%	45.9-50.5°C 20.7%
	Green roof Predicted LST			
	-5.21 to -3.91°C 0.5%	-3.91 to -2.61°C 0.8%	-2.61 to -1.30°C 0.7%	-1.30 to 0°C 98.0%
	Temperature reduction			

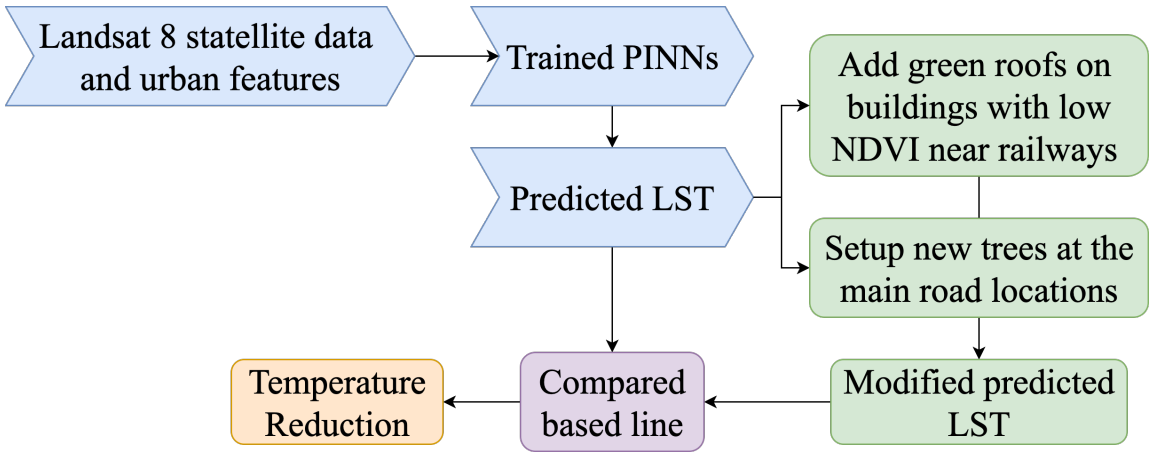

Fig. 16. Schematic of the integrated strategy for deploying new trees and green roofs to mitigate urban heat

in Bologna (accounting for 39.6% of the 2,288 rail-adjacent structures) and 259 in Washington D.C. (36.5% of the 709 buildings near railway corridors).

Concurrently, new trees were deployed along main transportation corridors to leverage their dual cooling mechanisms—shading impervious surfaces and enhancing evapotranspiration—thereby counteracting heat accumulation from vehicular activity. Main roads were identified using OpenStreetMap's hierarchical classification system, targeting major transportation arteries while excluding local streets and minor pathways. This classification included motorways, trunk roads, primary roads, and secondary roads, capturing the principal transportation network carrying significant traffic volumes.

The tree planting strategy employed city-specific proportional approaches, with new trees randomly distributed along main roads while incorporating spatial constraints to avoid infrastructure conflicts. Tree placement avoided traffic light locations, identified through direct queries to OpenStreetMap for features tagged as 'traffic signals', and excluded areas where railways intersected with main roads as well as locations with existing trees. In Bologna, a conservative 2% expansion rate was applied to the existing inventory of 19,182 trees, targeting 383 new plantings. Spatial constraints along main roads limited actual placement to 286 trees, achieving approximately 75% coverage through systematic spacing. Washington D.C. implemented a more ambitious 30% expansion relative to its smaller existing base of 608 trees, successfully placing all 182 target trees along main roads with optimised spacing of approximately 460 metres while maintaining these spatial constraints.

The integrated strategy employed enhanced vegetation parameters compared to the only green roof scenario detailed in Section 3.2. Where the previous analysis used $\mathrm{NDVI}_{\mathrm{GRs}} = 0.65$ for green roofs alone, the integrated approach used new NDVI = 0.7 for both green roofs and newly planted trees. This elevated value reflects the combined effect of mature vegetation systems: well-established green roofs with deeper substrate and higher plant density, complemented by the full canopy development of newly planted trees. The higher new NDVI value accounts for the increased biomass, leaf area index, and consequent enhanced cooling capacity of this more comprehensive greening approach.

Emissivity values were dynamically computed using the established vegetation fraction model (see in Eq. 25). Building polygons were rasterised and pixel values systematically updated to simulate intervention effects. For green roofs, the algorithm performed pixel-level replacement across building footprints, substituting original NDVI values with 0.7 and updating emissivity accordingly. For tree planting, linear buffers along main roads received similar vegetation enhancements. This raster-based approach ensured comprehensive coverage while maintaining spatial alignment with the original urban feature datasets. The modified NDVI and emissivity arrays subsequently served as input for the physics-informed neural network, enabling accurate

prediction of thermal impacts while preserving spatial integrity.

3.3.2. Targeting Analysis

Fig. 17 shows how integrated urban greening strategies are put into practice in Bologna (a) and Washington, D.C. (b), with a focus on targeted deployment along thermal vulnerability corridors. The map details three principal interventions: new trees (green triangles) planted along main roads (red lines); green roofs (yellow squares) installed on buildings with NDVI ≤ 0.2 near railways (dashed purple lines); and traffic lights (yellow stars) positioned as additional infrastructure nodes. Crucially, the chosen buildings feature low vegetation cover (NDVI ≤ 0.2) and high emissivity values (Bologna: 0.969 in Fig. 18; D.C.: 0.965 in Fig. 19), confirming their role as localised heat accumulators. This targeting approach aligns with the study's vulnerability framework and marks a key shift from the reactive method of Fig. 11's LST-based targeting—which placed green roofs only within existing thermal extremes, leading to sparse, fragmented coverage of the most intense hotspots—to the proactive strategy of Fig. 14's UHTI-based targeting, which extends coverage across broader rail-adjacent zones of vulnerability, irrespective of current LST.

Unlike the narrow scope of Fig. 11, which focused solely on present thermal conditions, the deployment in Fig. 17 explicitly targets rail-adjacent buildings with NDVI ≤ 0.2. These are areas that LST-based targeting would miss, but which the UHTI framework recognises as critical for long-term heat resilience. Ultimately, this holistic strategy combines green roofs, tree planting, and infrastructure adaptation to address multi-layered urban heat vulnerabilities, with the dense clustering of green roofs near railways highlighting the focus on rail-adjacent zones as critical thermal hotspots.

Distribution analysis revealed distinct urban thermal signatures (Figs. 18& 19). Bologna exhibited a moderate negative correlation (r = -0.100) between NDVI and emissivity, suggesting that even sparse vegetation provides some thermal benefit. In contrast, Washington D.C. showed a positive correlation (r = 0.216), which may reflect its specific building materials or microclimates. Despite this difference, both cities demonstrated remarkably consistent emissivity in low-vegetation areas. For Bologna, the emissivity of low-NDVI buildings was tightly clustered (mean = 0.969), confirming uniform radiative properties for its historic impervious surfaces. Similarly, in D.C., low-NDVI buildings showed constrained variability (mean = 0.965). This consistent emissivity in both cities' hotspots—despite their differing correlations—underscores that these zones have predictable radiative behaviour. This predictability makes them ideal targets for green infrastructure, as interventions like green roofs can be expected to produce reliable cooling effects.

Fig. 17. Spatial implementation of urban greening: a) Bologna and b) Washington, D.C., showing new trees (green triangles) along main roads (red lines), green roofs (yellow squares) on buildings with NDVI ≤ 0.2 near railways (dashed purple), and traffic lights (yellow stars).

3.3.3. Thermal Impact Results

Fig. 20 quantifies the synergistic thermal impact of integrated greening (combining trees and green roofs) in Bologna and Washington, D.C., revealing a marked improvement over single-intervention strategies (Figs. 15 and 13). In Bologna, the combined strategy achieves a maximum temperature reduction (ΔT) of -6.06°C (Fig. 20c), with 97.4% of pixels experiencing some cooling (Fig. 20f)—a broader spa-

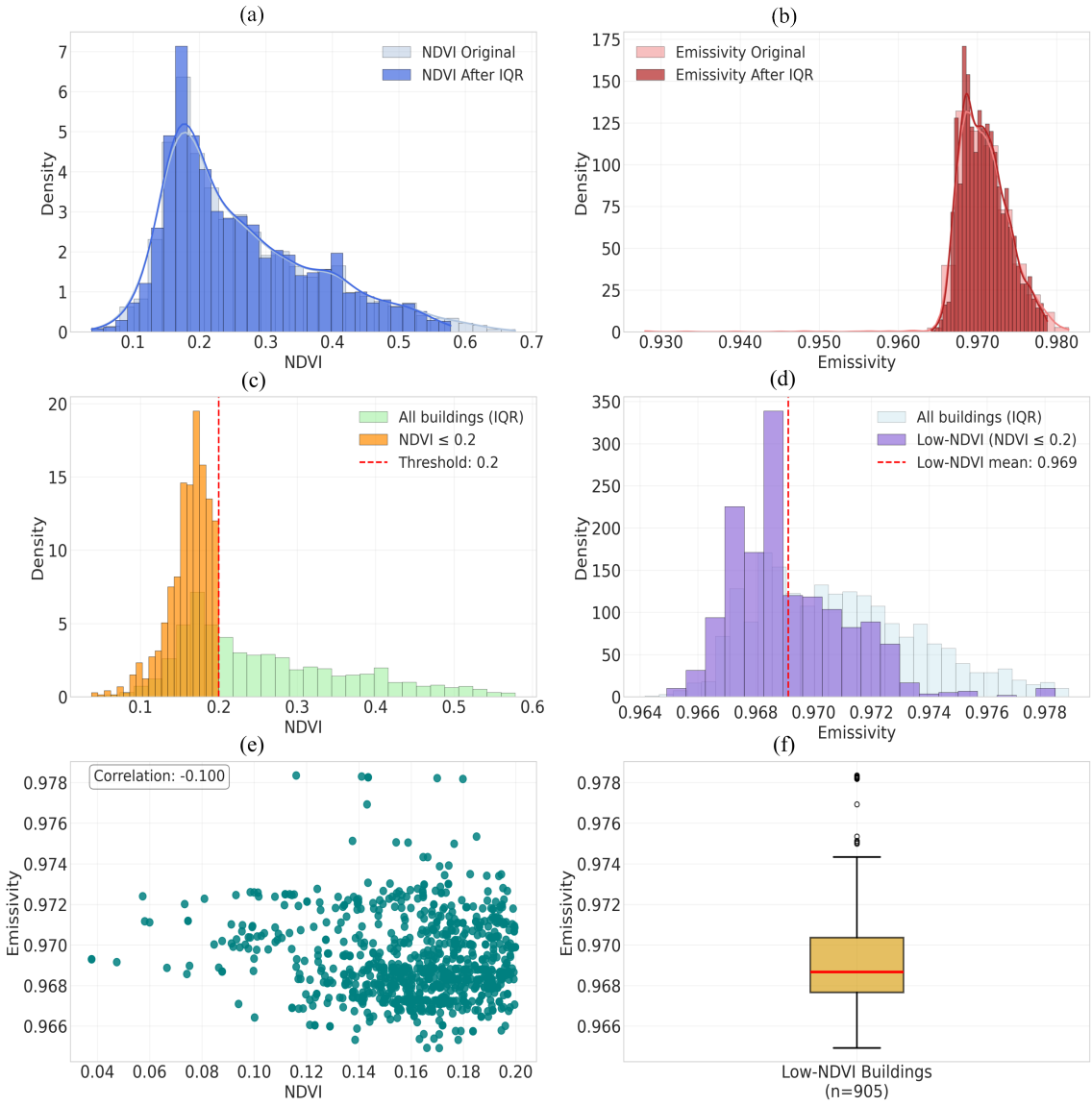

Fig. 18. Bologna building NDVI and emissivity analysis near railways: a) NDVI distributions before (light blue) and after (blue) IQR filtering; b) Emissivity distributions before (pink) and after (red) IQR filtering; c) NDVI histogram with $\leq$0.2 threshold (dashed red); d) Emissivity histogram for low-NDVI buildings (purple) with mean (dashed red); e) NDVI-emissivity scatter plot (correlation: -0.100); f) Emissivity boxplot for low-NDVI buildings (n=905), showing consistent values and outliers.

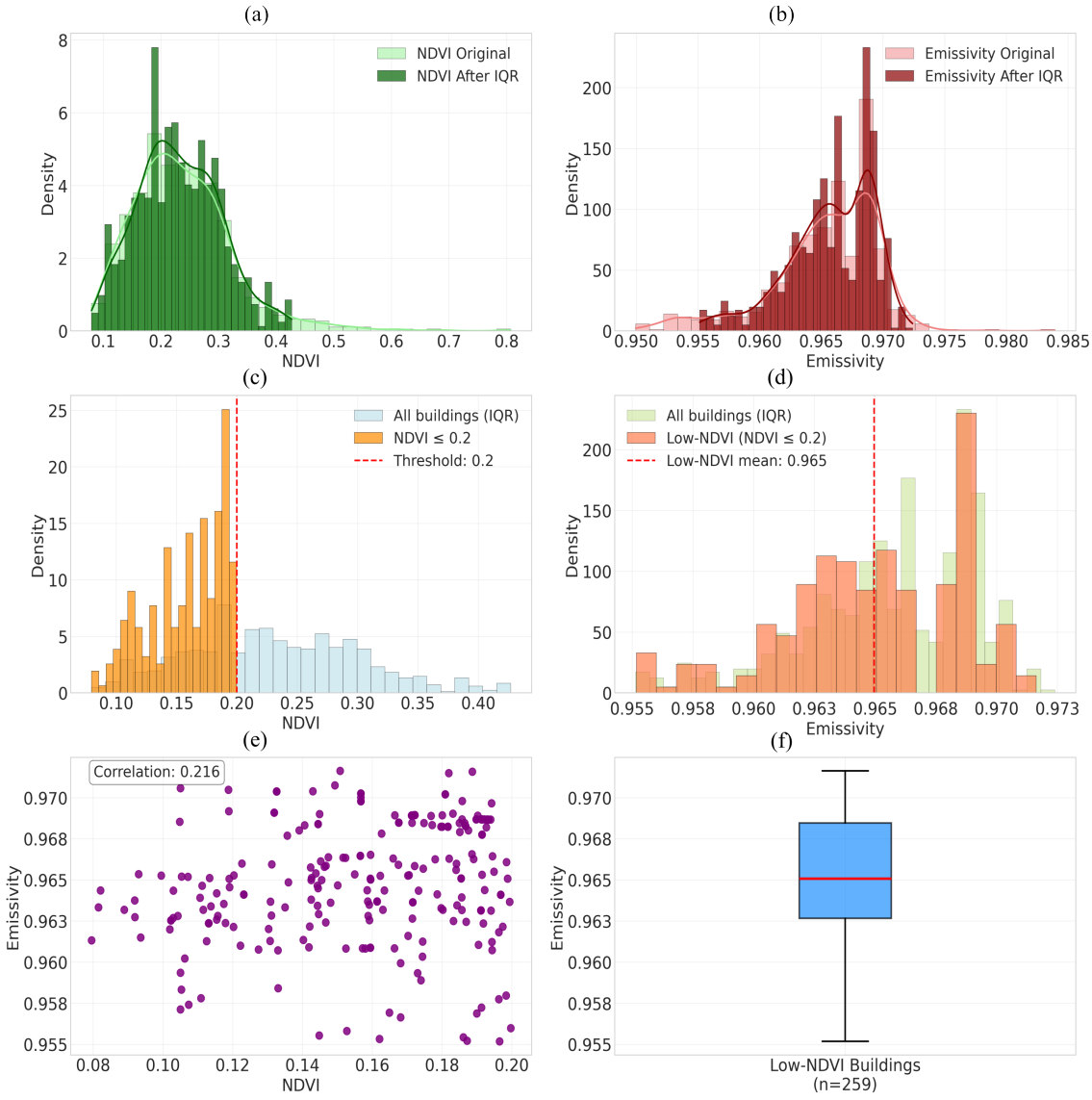

Fig. 19. Washington, D.C. building NDVI and emissivity analysis near railways: a) NDVI distributions before (light green) and after (green) IQR filtering; b) Emissivity distributions before (pink) and after (red) IQR filtering; (c) NDVI histogram with $\leq$0.2 threshold (dashed red); (d) Emissivity histogram for low-NDVI buildings (salmon) with mean (dashed red); e) NDVI-emissivity scatter plot (correlation: 0.216); f) Emissivity boxplot for low-NDVI buildings (n=259), highlighting uniformity and central tendency.

tial impact than that of green roofs alone (Fig. 15), where non-rail UHTI hotspots achieved 95.9% cooling but only 2.3% of pixels reached -6.64°C. The histogram in Fig. 20e shows a reduction in high-temperature pixels (the 45.8–49.3°C range dropping from 7.6% to 6.7% in Bologna), whereas Fig. 15's green roof-only non-rail hotspots reduced the range (45.8–49.6°C) from 5.7% to 5.2% (Table 5), indicating that integrated greening more effectively suppresses extreme heat while expanding the footprint of moderate cooling.

For D.C., the integrated strategy yields a stronger localised cooling effect (max ΔT = -7.19°C, Fig. 20i), surpassing both Fig. 15's green roof-only rail-buildings (-5.21°C) and Fig. 13's LST-only rail-adjacent targeting (max $\Delta T \approx$ -1.3°C). The histogram in Fig. 20k shows D.C.'s hottest LST range (45.9–50.5°C) declining from 22.2% to 21.0% with combined greening, whereas Fig. 13's rail-adjacent LST hotspots (Fig. 13l) failed to reduce this range meaningfully (violin plot median $\Delta T \approx 0$°C). Critically, Fig. 20's temperature reduction distribution (Fig. 20l) shows 98.3% of pixels cooled by at least -1.80°C, contrasting sharply with Fig. 13's rail-adjacent results, where 98.7% of pixels showed negligible cooling ($\Delta T \approx 0$°C).

The comparison underscores two key advances over prior approaches. Firstly, the integrated strategy does not simply sum green roof and tree impacts but creates synergistic cooling—evident in D.C.'s -7.19°C max ΔT, which exceeds Fig. 15's -5.21°C (green roofs alone) and likely incorporates tree-induced shading and evapotranspiration. Secondly, while Fig. 13's LST-only rail-adjacent targeting yielded minimal cooling (due to focusing only on existing thermal extremes), Fig. 20's integrated approach, by targeting vulnerability (via UHTI, as in Fig. 15) and leveraging multi-layered greening, achieves meaningful mitigation in rail-adjacent zones. For example, Bologna's rail-buildings in Fig. 15 (Table 5) showed 0.3% of pixels at -4.96°C, whereas Fig. 20's combined strategy achieves -6.06°C in non-rail zones—implying rail-adjacent areas would also benefit from this enhanced cooling profile.

Overall, Fig. 20 demonstrates that integrated greening overcomes the limitations of single-intervention frameworks (Figs. 15 and 13) by expanding the spatial extent of cooling, deepening temperature reduction in extreme heat zones, and effectively targeting rail-adjacent vulnerabilities in which LST-only methods (Fig. 13) and green roof-only strategies (Fig. 15) underperform. This positions multi-layered nature-based solutions as a more robust strategy for comprehensive urban heat resilience. The consistent alignment between cooling patterns and intervention locations validates the NDVI ≤ 0.2 selection criterion, while the complementary statistical shifts in LST distributions underscore the efficacy of targeted, modest greening investments for urban heat mitigation across diverse urban contexts.

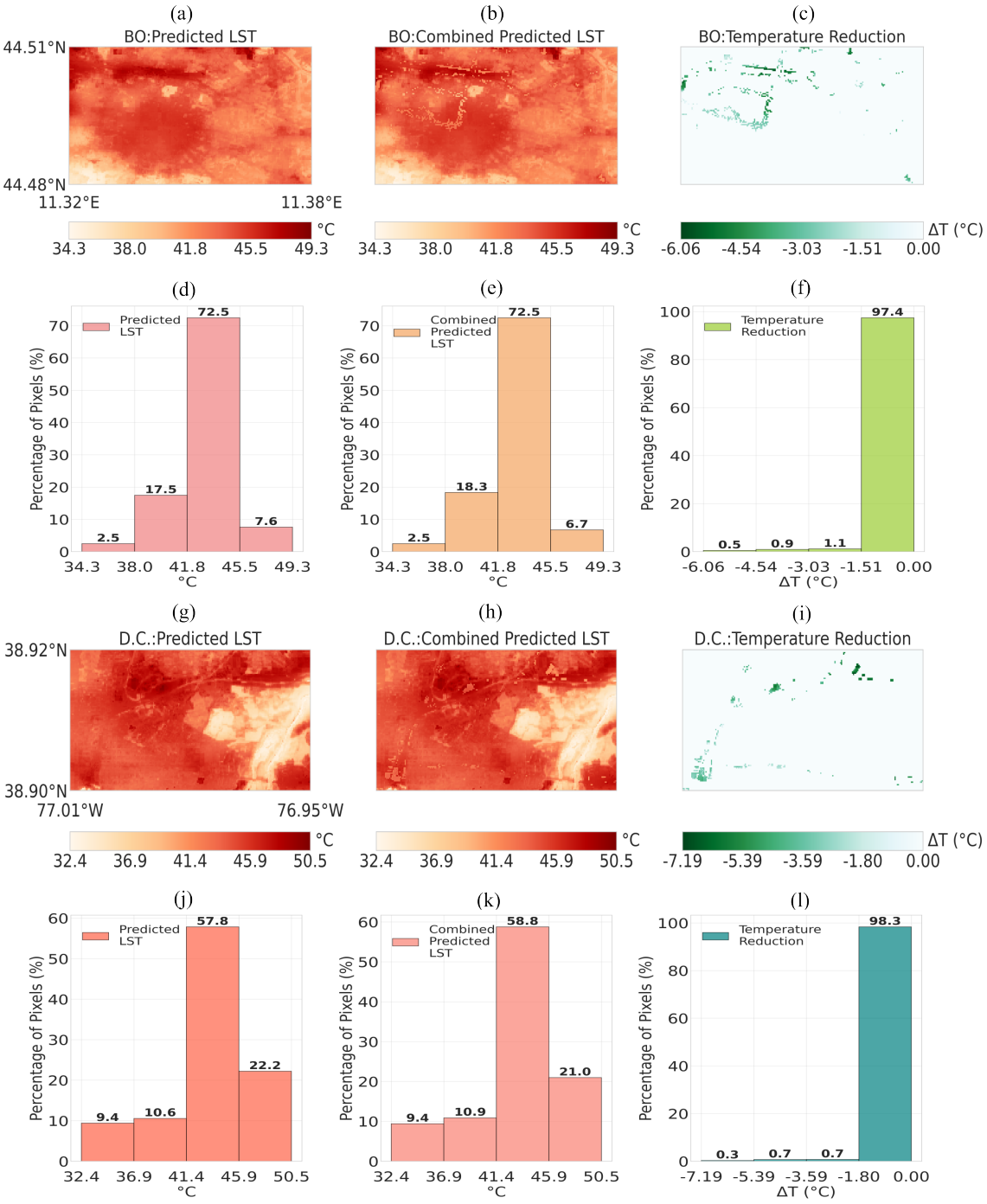

Fig. 20. Thermal impact of integrated greening strategy in Bologna (a–f) and D.C. (g–l), showing predicted LST, combined intervention effects, temperature reductions, and distribution statistics.

4. Discussion

4.1. Limitations of Data and the Challenge of Missing Values

A well-documented challenge in using satellite data for urban modelling is the prevalence of missing values (NaN) in critical parameters such as LST, NDVI, and emissivity. These gaps arise primarily from atmospheric interference (e.g., cloud cover, aerosol scattering) and sensor-specific limitations (Mitraka et al., 2012; Li et al., 2022). To ensure the initial integrity of our PINN models, we adopted a conservative approach by selecting a contiguous urban sub-region with complete data, thereby excluding pixels containing NaN values. Whilst this provided a stable foundation for developing and validating our core methodology, it inherently limits the spatial scope of our analysis and may introduce selection bias by omitting areas systematically affected by cloud cover.

A particularly suitable candidate for future work is the Data Interpolating Empirical Orthogonal Functions (DINEOF) method, widely used in oceanography and climatology (Alvera-Azcárate et al., 2011). DINEOF reconstructs missing data by identifying the dominant spatial and temporal covariance modes in a dataset, requiring no a priori knowledge of the statistics, which makes it ideal for gridded satellite data (Beckers & Rixen , 2003). The adoption of such techniques, including emerging deep learning imputation methods (Yan, 2024), would be a logical next step to enhance the comprehensiveness of future urban analyses.

4.2. Distinction Between Land Surface and Air Temperature

A key limitation of this study is its reliance on LST to quantify the urban heat island effect. Although LST is a valuable measure of surface energy balance, it does not directly represent the human thermal experience, which is more accurately captured by ambient air temperature (Tair) at street level (Tzavali et al., 2015). The relationship between the two is complex and mediated by factors including surface roughness, wind speed, and humidity. For instance, a sun-exposed asphalt surface may have a very high LST but may not efficiently heat the surrounding air if ventilation is strong. Conversely, a densely built area with a moderate LST might trap heat, leading to significantly higher and more hazardous air temperatures.

This distinction is critical for urban policy. Public health warnings and energy consumption models are based predominantly on air temperature. Our analysis, focused on summer conditions, effectively identifies "surface heat islands," which are useful for understanding thermal stress on infrastructure. However, the classic "atmospheric heat island," measured as the canopy-layer air temperature difference, can exhibit different spatial patterns and intensities. Consequently, a policy based

solely on LST risks misallocating resources; for example, it might prioritise cooling a hot, open car park over a shaded but poorly ventilated courtyard where the actual human exposure to heat is greater.

Multiple studies confirm that LST and Tair are not interchangeable and can exhibit weak or context-dependent correlations. Fahy et al. (2025) explicitly state that "LST is poorly correlated with air temperature" in the context of thermal comfort. Similarly, Yang et al. (2020) show that UHI intensity estimates vary considerably depending on the metric used, with surface-based measures potentially misrepresenting human-experienced heat stress.

To bridge this gap, future research should integrate complementary data sources. A promising approach is to combine satellite-derived LST with ground-based Tair sensor networks, providing a direct link to human-scale conditions Jaiswal et al. (2023). Furthermore, integrating Urban Canopy Models (UCMs) could simulate the complex interactions between the surface and the atmosphere by accounting for building geometry, anthropogenic heat, and vegetation effects (Hamdi et al., 2020). Such integrated models are essential for evaluating policy interventions, as building geometry and anthropogenic heat fluxes play a critical role in local climate outcomes (Morales et al., 2025).

4.3. Model Sensitivities and Physical Limitations

The analysis reveals a significant sensitivity to certain input parameters. For instance, adjusting the assigned NDVI for green roofs from 0.65 to 0.7 produced substantial variation in predicted cooling. This underscores a critical challenge for practical application: the model's performance is contingent upon a highly accurate, site-specific characterisation of urban materials and vegetation. This requirement is complicated by the temporal variability of parameters like NDVI, which fluctuate with seasonal cycles and plant health—a dynamic our current static framework does not capture.

This observed sensitivity aligns with a recognised challenge in PINNs. Recent work by Chen et al. (2025) demonstrates that PINN performance is highly sensitive to hyperparameters and physical constants, noting that even minor inaccuracies in thermal properties can propagate into significant prediction errors. This is particularly problematic in urban contexts, where material properties exhibit fine-scale heterogeneity.

A primary limitation of the present study is the fixed parameterisation of the heat source term, Q (Eq. 11). While its linear formulation, with coefficients derived from literature, successfully encapsulates essential urban thermal mechanisms, it remains a simplified abstraction. The model in its current form cannot adjust these weights

based on local observational data.

Consequently, a critical direction for future work is to adopt a hybrid approach that transitions from a fixed to a learnable Q term (Zhao et al., 2023). By treating the coefficients α_1 to α_8 as trainable parameters within the PINN frameworks, the model could calibrate their magnitudes directly from data. To enhance robustness, this could be combined with Bayesian regularisation, which would prevent overfitting by incorporating uncertainty quantification into the learning process (Yang et al., 2021; Lynda et al., 2025). This methodology would enable the model to discover the precise contribution of each urban feature to the local heat budget, leading to more data-driven and physically consistent predictions.

Moreover, the model does not explicitly resolve processes critical to green infrastructure performance, such as evapotranspiration (ET) and latent heat flux. Urban climate literature consistently emphasises that urban surface temperature cannot be modelled accurately without resolving the full surface energy balance (Oke, 1988). Evapotranspiration is a dominant cooling mechanism: "water bodies and vegetation exert significant cooling effects through evapotranspiration, lowering ambient temperatures by 1°C to 4°C" (Bai & Xing, 2025). By omitting ET, our current PINN treats green roofs as merely high-albedo surfaces, missing their primary biophysical function. Consequently, the model's robustness is tied to the accuracy of its input parameters as proxies for these missing physics.

4.4. Future Directions and Model Evolution

A primary limitation of this study is its steady-state modelling framework, which analyses urban heat patterns from a single snapshot in time. This approach does not account for the dynamic processes central to the urban thermal environment, such as diurnal cycles, seasonal variations in vegetation phenology, or the influence of transient weather conditions like wind, humidity, and cloud cover. Consequently, the model's applicability is restricted to summer daytime LST patterns, and its findings should not be generalised to represent night-time phenomena or year-round climate benefits. This temporal simplification limits the model's utility for real-time applications or seasonal urban planning.

Addressing this by evolving the framework into a time-dependent model is a critical next step. Future work should implement PINNs that incorporates a temporal derivative term ($\partial T/\partial t$) to resolve transient heat dynamics (Bonab et al., 2025). Such a development would require, and be well-suited to, multi-temporal satellite data from sources like Landsat or MODIS. This enhanced spatiotemporal capability would provide valuable insights into the evolution of urban heat islands under changing conditions, a direction strongly supported by studies analysing long-term satellite

records (Fang et al., 2024).

A particularly promising application of PINNs lies in their capacity for solving inverse problems to identify key drivers of urban environmental phenomena. Our framework could be extended to quantify the relative contributions of different urban morphologies (e.g., building density, transport networks) to thermal anomalies through Bayesian inference. This aligns with emerging methodologies; for example, (Cuomo et al., 2022) highlight that PINNs can solve inverse problems namely identifying unknown source terms from sparse data. Recent hybrid Bayesian-PINN frameworks have been developed to infer UHI drivers while quantifying uncertainty (Lynda et al., 2025), which would enable urban planners to prioritise intervention strategies by identifying the most significant factors exacerbating urban heat islands.

Furthermore, the framework could be expanded to model synergistic systems, such as the integration of green roofs with photovoltaic (PV) panels. Research indicates significant mutual benefits: vegetation reduces ambient temperatures to improve PV efficiency, while panels provide shading that influences plant growth. Schindler et al. (2018) further demonstrate that green roofs directly reduce PV panel temperatures, enhancing electrical output. A coupled PINN framework that simultaneously models thermal regulation and energy production would provide valuable insights for optimising these integrated systems.

From an architectural perspective, substituting fully connected networks with Convolutional Neural Networks (CNNs) represents a logical evolution for processing satellite data (Zhang et al., 2025). CNNs offer inherent advantages for analysing spatially structured data through localised filters, weight sharing, and hierarchical feature extraction. These attributes align perfectly with the raster format of satellite imagery, enabling more efficient learning of spatial patterns and naturally accommodating translation invariance—a critical property for urban analysis.

5. Conclusions

This study has successfully developed and validated a novel PINN framework for urban heat island mitigation, representing a significant advance over conventional data-driven or purely physical modelling approaches. By integrating high-resolution satellite imagery with vector-based urban morphology data within a model grounded in the principles of heat diffusion, we have created a predictive tool that is both accurate and physically consistent. The framework's application to two distinct cities—Bologna, Italy and Washington, D.C., USA—demonstrates its robustness and transferability. The model performed exceptionally well against Landsat 8 data, with R^2 values exceeding 0.92, and proved capable of identifying highly effective green

infrastructure interventions. These interventions achieved an extensive reduction of more than 97% in the area of thermal hotspots, coupled with substantial cooling effects—both in widespread moderate reductions (area-weighted averages of up to 1.8°C) and intense localised cooling exceeding 8°C—providing a powerful, evidence-based foundation for urban climate action.

The core contribution of this work is its methodological synergy. The development of a GeoJSON-to-tensor conversion pipeline addresses a critical gap in geospatial data fusion, enabling the simultaneous use of raster-based environmental parameters and vector-based infrastructural features. More profoundly, by embedding the heat equation directly into the learning process, the PINN frameworks ensure its predictions are constrained by the laws of thermodynamics, not just statistical correlations. This moves urban climate modelling beyond "black box" predictions towards explainable, scientifically grounded simulations. Consequently, the model outputs are not merely predictions but actionable insights, allowing planners to strategically balance ecological benefits with infrastructural demands.

In conclusion, this research provides a scalable and replicable blueprint for data-driven urban planning. The findings demonstrate that targeted, rather than blanket, greening strategies can yield disproportionate cooling benefits—achieving both broad moderate temperature reductions and dramatic localised cooling—a crucial insight for optimising limited municipal budgets and maximising community resilience. By prioritising heat-vulnerable zones for intervention, the framework directly supports the development of more equitable and sustainable cities. This work firmly positions PINNs as a transformative technology in the urban climate toolkit, offering a path forward to not only understand but also actively mitigate the pressing challenges of urban warming.

Data availability statement

Landsat 8 satellite data were sourced from Google Earth Engine (`https://earthengine.google.com/`), while urban morphology data were obtained using the OSMnx library in Python (`https://pypi.org/project/osmnx/1.3.1/`). The Python code developed for this study has been made publicly available on Zenodo (`https://zenodo.org/records/17385260`).

Acknowledgments

The authors did not receive any external funding for this work.

Conflicts of Interest

The authors declare that they have no known competing financial interests or personal relationships that could have appeared to influence the work reported in this document.

References

Ahmed, A.N., Aldahoul, N., Aziz, N.A., Huang, Y.F., Sherif, M. and El-Shafie, A., (2025). The urban heat Island effect: A review on predictive approaches using artificial intelligence models. *City and Environment Interactions*, p.100234.

Alvera-Azcárate, A., Barth, A., Sirjacobs, D., Lenartz, F. and Beckers, J.M., (2011). Data Interpolating Empirical Orthogonal Functions (DINEOF): a tool for geophysical data analyses. *Mediterranean Marine Science*, pp.5-11.

Arabi, R., Shahidan, M.F., Kamal, M.M., Jaafar, M.F.Z.B. and Rakhshandehroo, M., (2015). Mitigating urban heat island through green roofs. *Current World Environment*, 10(1), pp.918-927.

Bai, Y. and Xing, Y., (2025). Harnessing Green Infrastructure for Urban Heat Island Mitigation: Evidence-Based Strategies for Sustainable and Climate-Resilient Cities. *Sustainable Cities and Society*, p.106843.

Baqa, M.F., Lu, L., Guo, H., Song, X., Alavipanah, S.K., Nawaz-ul-Huda, S., Li, Q. and Chen, F., (2025). Investigating heat-related health risks related to local climate zones using SDGSAT-1 high-resolution thermal infrared imagery in an arid megacity. *International Journal of Applied Earth Observation and Geoinformation*, 136, p.104334.

Beckers, J.M. and Rixen, M., (2003). EOF calculations and data filling from incomplete oceanographic datasets. *Journal of Atmospheric and oceanic technology*, 20(12), pp.1839-1856.

Boeing, G. (2017). OSMnx: New methods for acquiring, constructing, analyzing, and visualizing complex street networks. *Computers, environment and urban systems*, 65, pp.126-139.

Bonab, S.A., Song, W. and Yazdani-Asrami, M., (2025). Physics-informed neural network model for transient thermal analysis of superconductors. *Superconductor Science and Technology*, 38(8), p.08LT01.

Botarelli, T., Fanfani, M., Nesi, P. and Pinelli, L., (2025). Using Physics-Informed neural networks for solving Navier-Stokes equations in fluid dynamic complex scenarios. *Engineering Applications of Artificial Intelligence*, 148, p.110347.

Bowman, B., Oian, C., Kurz, J., Khan, T., Gil, E. and Gamez, N., (2023). Physics-informed neural networks for the heat equation with source term under various boundary conditions. *Algorithms*, 16(9), p.428.

Butler, H., Daly, M., Doyle, A., Gillies, S., Hagen, S. and Schaub, T., (2016). The geojson format. *Internet Engineering Task Force (IETF)*.

Cai, S., Mao, Z., Wang, Z., Yin, M. and Karniadakis, G.E., (2021). Physics-informed neural networks (PINNs) for fluid mechanics: A review. *Acta Mechanica Sinica*, 37(12), pp.1727-1738.

Chen, L., Fang, B., Zhao, L., Zang, Y., Liu, W., Chen, Y., Wang, C. and Li, J., (2022). DeepUrbanDownscale: A physics informed deep learning framework for high-resolution urban surface temperature estimation via 3D point clouds. *International Journal of Applied Earth Observation and Geoinformation*, 106, p.102650.

Chen, Y., Wang, H. and Chen, Z., (2025). Sensitivity analysis of physical regularization in physics-informed neural networks (PINNs) of building thermal modeling. *Building and Environment*, 273, p.112693.

Ching, G.N., Yik, S.K., Heng, S.L., Ho, B.H., Crank, P.J., Mandelmilch, M., Ho, X.T. and Chow, W.T., (2025). Park cool island modifications to assess radiative cooling of a tropical urban park. *Scientific Reports*, 15(1), p.15355.

Cipolla, S.S., Maglionico, M., Semprini, G., Villani, V. and Bonoli, A., (2017). Green roofs as a strategy for urban heat island mitigation in Bologna (Italy). *In International Symposium on Greener Cities for More Efficient Ecosystem Services in a Climate Changing World 1215* (pp. 295-300).

Cleland, S.E., Steinhardt, W., Neas, L.M., West, J.J. and Rappold, A.G., (2023). Urban heat island impacts on heat-related cardiovascular morbidity: A time series analysis of older adults in US metropolitan areas. *Environment international*, 178, p.108005.

Cuce, P.M., Cuce, E. and Santamouris, M., (2025). Towards sustainable and climate-resilient cities: mitigating urban heat islands through green infrastructure. *Sustainability*, 17(3), p.1303.

Cui, Y.Y. and De Foy, B., (2012). Seasonal variations of the urban heat island at the surface and the near-surface and reductions due to urban vegetation in Mexico City. *Journal of Applied Meteorology and Climatology*, 51(5), pp.855-868.

Cuomo, S., Di Cola, V.S., Giampaolo, F., Rozza, G., Raissi, M. and Piccialli, F., (2022). Scientific machine learning through physics–informed neural networks: Where we are and what's next. *Journal of Scientific Computing*, 92(3), p.88.

Debbage, N. and Shepherd, J.M., (2015). The urban heat island effect and city contiguity. *Computers, Environment and Urban Systems*, 54, pp.181-194.

Eivazi, H., Wang, Y. and Vinuesa, R., (2024). Physics-informed deep-learning applications to experimental fluid mechanics. *Measurement science and technology*, 35(7), p.075303.

Elbeltagi, A., Vishwakarma, D.K., Katipoğlu, O.M., Sushanth, K., Heddam, S., Singh, B.P., Shukla, A., Gautam, V.K., Pande, C.B., Hussain, S. and Ghosh, S., (2025). Air temperature estimation and modeling using data driven techniques based on best subset regression model in Egypt. *Scientific Reports*, 15(1), p.20200.

Ermida, S. L. and Soares, P. and Mantas, V. and Göttsche, F. M. and Trigo, I. F. (2020). Google earth engine open-source code for land surface temperature estimation from the landsat series. *Remote Sensing*, 12(9), p.1471.

Eyni, A., Zaitchik, B.F., Hobbs, B.F., Hadjimichael, A. and Shi, R., (2025). Distributional outcomes of urban heat island reduction pathways under climate extremes. *Scientific reports*, 15(1), p.9594.

Fang, Q., Liu, C., Ren, Z., Fu, Y., Fan, H., Wang, Y. and Yu, Z., (2024). Spatiotemporal Analysis of Surface Urban Heat Island Dynamics in Central Yunnan City Cluster. *Sustainability*, 16(11), p.4819.

Fahy, J.C., Bachofen, C., Camponovo, R., Gallinelli, P. and Schlaepfer, M.A., (2025). Beyond land surface temperature: Identifying areas of daytime thermal discomfort in cities by combining remote sensing and field measurements. *Urban Climate*, 61, p.102460.

Gartland, L.M., (2010). Heat islands: understanding and mitigating heat in urban areas. *Routledge Press: London, UK, 2010*.

Ghaffari, Z., (2021). Assessing the Impact of Green Roof on the Urban Heat Island Using Satellite Images: A Case Study of Washington DC. *Texas State University-San Marcos*.

Gorelick, N. and Hancher, M. and Dixon, M. and Ilyushchenko, S. and Thau, D. and Moore, R. (2017). Google Earth Engine: Planetary-scale geospatial analysis for everyone. *Remote sensing of Environment*, 202, pp.18-27.

Hamdi, R., Kusaka, H., Doan, Q.V., Cai, P., He, H., Luo, G., Kuang, W., Caluwaerts, S., Duchêne, F., Van Schaeybroek, B. and Termonia, P., (2020). The state-of-the-art of urban climate change modeling and observations. *Earth Systems and Environment*, 4(4), pp.631-646.

Ho, J.Y., Shi, Y., Lau, K.K., Ng, E.Y., Ren, C. and Goggins, W.B., (2023). Urban heat island effect-related mortality under extreme heat and non-extreme heat scenarios: A 2010–2019 case study in Hong Kong. *Science of The Total Environment*, 858, p.159791.

Hulley, G. C. and Hook, S. J. and Abbott, E. and Malakar, N. and Islam, T. and Abrams, M. (2015). The ASTER Global Emissivity Dataset (ASTER GED): Mapping Earth's emissivity at 100 meter spatial scale. *Geophysical Research Letters*, 42(19), pp.7966-7976.

Jaiswal, N., Deb, S.K. and Kishtawal, C.M., (2023). Development of a hybrid model to predict air temperature over an urban area: A case study over Ahmedabad, India. *Atmospheric Research*, 292, p.106876.

Kalnay, E. and Kanamitsu, M. and Kistler, R. and Collins, W. and Deaven, D. and Gandin, L. and Iredell, M. and Saha, S. and White, G. and Woollen, J. and others (2018). The NCEP/NCAR 40-year reanalysis project. *In Renewable energy* (pp. Vol1 146-Vol1 194).

Khosravi, K., Pham, B.T., Chapi, K., Shirzadi, A., Shahabi, H., Revhaug, I., Prakash, I. and Bui, D.T., (2018). A comparative assessment of decision trees algorithms for flash flood susceptibility modeling at Haraz watershed, northern Iran. *Science of the Total Environment*, 627, pp.744-755.

Kim, S.W. and Brown, R.D., (2021). Urban heat island (UHI) intensity and magnitude estimations: A systematic literature review. *Science of the Total Environment*, 779, p.146389.

Kim, S., Jeong, M. and Ko, B.C., (2022). Lightweight surrogate random forest support for model simplification and feature relevance. *Applied Intelligence*, 52(1), pp.471-481.

Kingma, D. P. and Ba, J. (2014). Adam: A method for stochastic optimization. *arXiv preprint arXiv:1412.6980*.

Knight, T., Price, S., Bowler, D., Hookway, A., King, S., Konno, K. and Richter, R.L., (2021). How effective is 'greening'of urban areas in reducing human exposure to ground-level ozone concentrations, UV exposure and the 'urban heat island effect'? An updated systematic review. *Environmental Evidence*, 10(1), p.12.

Łach, Ł. and Svyetlichnyy, D., (2025). Advances in numerical modeling for heat transfer and thermal management: a review of computational approaches and environmental impacts. *Energies*, 18(5), p.1302.

Li, Z.L., Tang, B.H., Wu, H., Ren, H., Yan, G., Wan, Z., Trigo, I.F. and Sobrino, J.A., (2013). Satellite-derived land surface temperature: Current status and perspectives. *Remote sensing of environment*, 131, pp.14-37.

Li, X., Zhou, Y., Yu, S., Jia, G., Li, H. and Li, W., (2019). Urban heat island impacts on building energy consumption: A review of approaches and findings. *Energy*, 174, pp.407-419.

Li, Z., Shen, H., Weng, Q., Zhang, Y., Dou, P. and Zhang, L., (2022). Cloud and cloud shadow detection for optical satellite imagery: Features, algorithms, validation, and prospects. *ISPRS Journal of Photogrammetry and Remote Sensing*, 188, pp.89-108.

Li, K. and Wang, H., (2025). Spatial and Data-Driven Approaches for Mitigating Urban Heat in Coastal Cities. *Buildings*, 15(19), p.3544.

Lin, L., Zhao, Y. and Zhao, J., (2025). Optimizing urban green space spatial patterns for thermal environment improvement: A multi-objective approach in the context of urban renewal. *Computers, Environment and Urban Systems*, 121, p.102320.

Lopes, H.S., Vidal, D.G., Cherif, N., Silva, L. and Remoaldo, P.C., (2025). Green infrastructure and its influence on urban heat island, heat risk, and air pollution: A case study of Porto (Portugal). *Journal of Environmental Management*, 376, p.124446.

Lu, Y., Shao, Z. and Lu, H., (2024). Quantification of anthropogenic heat and simulation of its effects on environment and climate: A comprehensive review. *Renewable and Sustainable Energy Reviews*, 204, p.114802.

Lynda, D., Logeswari, G., Tamilarasi, K. and Rakesh, S., (2025). Hybrid Bayesian deep learning model for predicting urban heat island intensity in African cities. *Scientific Reports*, 15(1), p.31280.

McCartney, S., Mehta, A., Shandas, V., Gallo, K., Paris, G., Nix, S., Quintero, T., Tomlinson, A. and Xian, G., (2020). Satellite Remote Sensing for Urban Heat Islands. *NASA Applied Remote Sensing Training Program (ARSET).*

Mihalakakou, G., Souliotis, M., Papadaki, M., Menounou, P., Dimopoulos, P., Kolokotsa, D., Paravantis, J.A., Tsangrassoulis, A., Panaras, G., Giannakopoulos, E. and Papaefthimiou, S., (2023). Green roofs as a nature-based solution for improving urban sustainability: Progress and perspectives. *Renewable and Sustainable Energy Reviews*, 180, p.113306.

Ming, Y., Liu, Y., Li, Y. and Song, Y., (2024). Unraveling nonlinear and spatial non-stationary effects of urban form on surface urban heat islands using explainable spatial machine learning. *Computers, Environment and Urban Systems*, 114, p.102200.

Mitraka, Z., Chrysoulakis, N., Kamarianakis, Y., Partsinevelos, P. and Tsouchlaraki, A., (2012). Improving the estimation of urban surface emissivity based on sub-pixel classification of high resolution satellite imagery. *Remote Sensing of Environment*, 117, pp.125-134.

Mondal, N., Anand, P., Khan, A., Deb, C., Cheong, D., Sekhar, C., Niyogi, D. and Santamouris, M., (2024). Systematic review of the efficacy of data-driven urban building energy models during extreme heat in cities: Current trends and future outlook. *In Building simulation, Beijing: Tsinghua University Press.* (Vol. 17, No. 5, pp. 695-722).

Morales, R.D., Audenaert, A. and Verbeke, S., (2025). Thermal comfort and indoor overheating risks of urban building stock-A review of modelling methods and future climate challenges. *Building and Environment*, 269, p.112363.

Nakata-Osaki, C.M., Souza, L.C.L. and Rodrigues, D.S., (2018). THIS–Tool for Heat Island Simulation: A GIS extension model to calculate urban heat island intensity based on urban geometry. *Computers, Environment and Urban Systems*, 67, pp.157-168.

Nardino, M. and Cremonini, L. and Crisci, A. and Georgiadis, T. and Guerri, G. and Morabito, M. and Fiorillo, E. (2022). Mapping daytime thermal patterns of Bologna municipality (Italy) during a heatwave: A new methodology for cities adaptation to global climate change. *Urban Climate*, 46, p.101317.

Oke, T.R., (1988). The urban energy balance. *Progress in Physical geography*, 12(4), pp.471-508.

Omrany, H. and Al-Obaidi, K.M., (2024). Application of digital twin technology for Urban Heat Island mitigation: review and conceptual framework. *Smart and Sustainable Built Environment*.

Oukawa, G.Y., Krecl, P. and Targino, A.C., (2022). Fine-scale modeling of the urban heat island: A comparison of multiple linear regression and random forest approaches. *Science of the total environment*, 815, p.152836.

Raissi, M., Perdikaris, P. and Karniadakis, G.E., (2019). Physics-informed neural networks: A deep learning framework for solving forward and inverse problems involving nonlinear partial differential equations. *Journal of Computational physics*, 378, pp.686-707.

Saaroni, H., Amorim, J.H., Hiemstra, J.A. and Pearlmutter, D., (2018). Urban Green Infrastructure as a tool for urban heat mitigation: Survey of research methodologies and findings across different climatic regions. *Urban climate*, 24, pp.94-110.

Sánchez-Cordero, F., Nanía, L., Hidalgo-García, D. and López-Chacón, S.R., (2025). Assessing the Spatial Benefits of Green Roofs to Mitigate Urban Heat Island Effects in a Semi-Arid City: A Case Study in Granada, Spain. *Remote Sensing*, 17(12), p.2073.

Schindler, B.Y., Blaustein, L., Lotan, R., Shalom, H., Kadas, G.J. and Seifan, M., (2018). Green roof and photovoltaic panel integration: Effects on plant and arthropod diversity and electricity production. *Journal of environmental management*, 225, pp.288-299.

Siddiqui, A., Maske, A.B., Khan, A., Kar, A., Bhatt, M., Bharadwaj, V., Kant, Y. and Hamdi, R., (2025). An Urban Climate Paradox of Anthropogenic Heat Flux and Urban Cool Island in a Semi-Arid Urban Environment. Atmosphere, 16(2).

Szymanowski, M. and Kryza, M., (2011). Application of geographically weighted regression for modelling the spatial structure of urban heat island in the city of Wroclaw (SW Poland). *Procedia Environmental Sciences*, 3, pp.87-92.

Thakur, A., Gupta, M., Sinha, D.K., Mishra, K.K., Venkatesan, V.K. and Guluwadi, S., (2024). Transformative breast Cancer diagnosis using CNNs with optimized ReduceLROnPlateau and Early stopping Enhancements. *International Journal of Computational Intelligence Systems*, 17(1), pp.1-18.

Tian, L., Lu, J., Li, Y., Bu, D., Liao, Y. and Wang, J., (2021). Temporal characteristics of urban heat island and its response to heat waves and energy consumption in the mountainous Chongqing, China. *Sustainable Cities and Society*, 75, p.103260.

Tzavali, A., Paravantis, J.P., Mihalakakou, G., Fotiadi, A. and Stigka, E., (2015). Urban heat island intensity: A literature review. *Fresenius Environmental Bulletin*, 24(12b), pp.4537-4554.

Venkatraman, S., Kandasamy, V., Rajalakshmi, J., Sabarunisha Begum, S. and Sujatha, M., (2024). Assessment of urban heat island using remote sensing and geospatial application: A case study in Sao Paulo city, Brazil, South America. *Journal of South American Earth Sciences*, 134, p.104763.

Wang, K., Jiang, S., Wang, J., Zhou, C., Wang, X. and Lee, X., (2017). Comparing the diurnal and seasonal variabilities of atmospheric and surface urban heat islands based on the Beijing urban meteorological network. *Journal of Geophysical Research: Atmospheres*, 122(4), pp.2131-2154.

Wang, J., Miao, S., Doan, Q.V., Chen, F., Abolafia-Rosenzweig, R., Yang, L., Zhang, G., Zhang, Y., Dou, J. and Xu, Y., (2023). Quantifying the impacts of high-resolution urban information on the urban thermal environment. *Journal of Geophysical Research: Atmospheres*, 128(6), p.e2022JD038048.

Xing, Z., Cheng, H. and Cheng, J., (2023). Deep learning method based on physics-informed neural network for 3D anisotropic steady-state heat conduction problems. *Mathematics*, 11(19), p.4049.

Yan, P., Li, Z., Ijaradar, J., Pape, S., Körner, M. and Wang, M., (2024). An imputation-enhanced hybrid deep learning approach for traffic volume prediction in urban networks: a case study in Dresden. *Data Science for Transportation*, 6(3), p.22.

Yang, H. and Liu, Y., (2005). A satellite remote sensing based assessment of urban heat island in Lanzhou city, northwest China. *International Archives of Photogrammetry. Netherlands: Remote Sensing and Spatial Information Sciences*, pp.1-6.

Yang, C., Yan, F. and Zhang, S., (2020). Comparison of land surface and air temperatures for quantifying summer and winter urban heat island in a snow climate city. *Journal of environmental management*, 265, p.110563.

Yang, L., Meng, X. and Karniadakis, G.E., (2021). B-PINNs: Bayesian physics-informed neural networks for forward and inverse PDE problems with noisy data. *Journal of Computational Physics*, 425, p.109913.

Yang, Y., Anderson, M., Knipper, K., Gao, F., Hain, C., Duan, W., Melton, F., Morton, C., Volk, J. and Wang, Z., (2024). Decreased Latency in Landsat Derived Evapotranspiration Products Using Machine Learning on Google Earth Engine. *In IGARSS 2024-2024 IEEE International Geoscience and Remote Sensing Symposium* (pp. 3054-3057).

Zang, Q.T., Wan, C.H.E.N. and Liang, X.J., (2013). Effects of evapotranspiration on mitigation of urban temperature by vegetation and urban agriculture. *Journal of Integrative Agriculture*, 12(8), pp.1307-1315.

Zhang, Z., Wan, C., Li, L., Pang, Y., Xiong, G., Zhang, C., Fan, X. and Wang, Y., (2025). CNN-IPINN: A method study on applying physics-informed neural networks to gear fault diagnosis. *Measurement Science and Technology.*

Zhao, X., Gong, Z., Zhang, Y., Yao, W. and Chen, X., (2023). Physics-informed convolutional neural networks for temperature field prediction of heat source layout without labeled data. *Engineering Applications of Artificial Intelligence*, 117, p.105516.

Zhao, Z., Wang, Y., Zhang, W., Ba, Z. and Sun, L., (2025). Physics-informed neural networks in heat transfer-dominated multiphysics systems: A comprehensive review. *Engineering Applications of Artificial Intelligence*, 157, p.111098.

Zipper, S.C., Schatz, J., Kucharik, C.J. and Loheide, S.P., (2017). Urban heat island-induced increases in evapotranspirative demand. *Geophysical Research Letters*, 44(2), pp.873-881.

Supplementary Appendix for:

Smart Urban Design with Physics-Informed Neural Networks: Quantifying Temperature Reductions from Green Infrastructures Using Satellite Thermal Data

Dung Thi Vu[a], Rafeeque Ahmed Nizamani[b], Abdul Ghafoor Nizamani[c,1]

[a] Istituto Nazionale di Geofisica e Vulcanologia, Sezione di Bologna, Viale Carlo Berti Pichat, 6/2, Bologna, 40127, BO, Italy

[b]School of Mechanical and Electronic Engineering, Wuhan University of Technology, Wuhan, Hubei, P.R. China
[c]Faculty of Computer Science, Engineering and Economics, Ostfold University College, BRA Veien 4, Halden, 1757, NO, Norway

[1]Corresponding: Abdul Ghafoor Nizamani (abdul.g.nizamani@hiof.no)

Appendix A: Hyperparameter Modification

Table A1: Hyperparameters for PINN Ablation Studies: Bologna and Washington, D.C.

This table presents the hyperparameter values tested in the ablation studies (Appendices A.1-A.4). All experiments used a fixed learning rate of 1×10^{-3} and a batch size of 512, consistent with the baseline model in Table 2. For each study, we varied the hyperparameter under investigation while keeping others constant. The constant values for a given experiment are highlighted in **bold**.

City	Experiment ID	Physics Weight (λ_1)	Boundary Weight (λ_2)	LeakyReLU Layers	Epochs
Bologna	A.1	**0.1**	0.5	**2**	10, 100, 300
	A.2	0.01, 1.0, 1.5	**0.3**	**2**	**300**
Washington D.C.	A.3	0.1	**0.3**	**2**	10, 100, 300
	A.4	0.01, 1.0, 1.5	**0.5**	**1**	**300**

Appendix A.1 presents an ablation study on the boundary weight for Bologna, using λ_2= 0.5. The results show a consistently dominant boundary loss across all epochs (a, c, e), confirming that this value is too high and forces the model to overfit the boundaries at the expense of predictive accuracy (b, d, f). This imbalance is evident from the early stages of training; after just 10 epochs (panel a), the boundary loss dominates the total loss, resulting in a high prediction error (panel b, maximum $\Delta T \approx 9.97°C$. However, a positive trend emerges with longer training. As the number of epochs increases to 100 and 300, the prediction maps show a progressive reduction in absolute differences, with the maximum ΔT decreasing to 8.45°C to 7.28°C respectively, despite the boundary loss remaining elevated. Although increasing training to 300 epochs partially mitigates the error, the fundamental imbalance remains. This pathology demonstrates the necessity of the lower, better-balanced value of λ_2= 0.3 used in our final experiments.

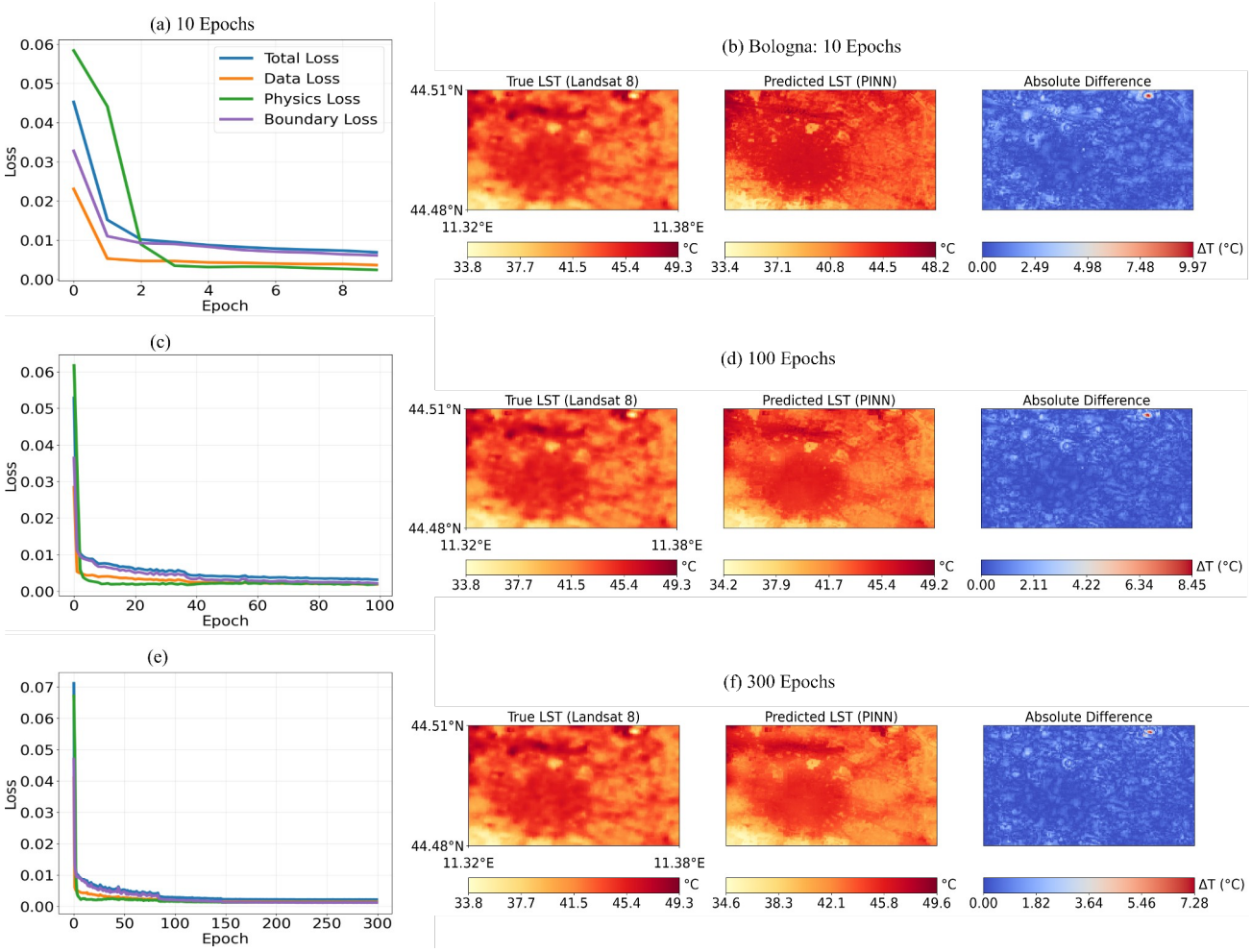

Appendix A. 1. *PINN model for Bologna with boundary weight λ_2 = 0.5: loss convergence (a, c, e) and land surface temperature (LST) prediction (b, d, f) at 10, 100, and 300 epochs.*

Appendix A.2 evaluates the model's performance for Washington D.C. using a boundary weight of λ_2= 0.3, revealing significant limitations in both loss balance and prediction accuracy.

In the initial training phase (10 epochs, subfigure a), the physics loss dominates over the data and boundary losses. This imbalance correlates directly with the predicted LST in subfigure (b), which shows distorted spatial patterns and a high maximum error ($\Delta T \approx 10.11°C$) compared to the Landsat 8 baseline. This suggests the model prioritises the physics-informed constraints at the expense of fitting the observed data, likely because the boundary condition is under-weighted.

As training progresses to 100 and 300 epochs (subfigures c and e), the loss curves stabilise. However, the corresponding prediction maps (d and f) show a systematic underestimation of surface temperatures, evident in their cooler colour scales. For instance, the minimum predicted temperature is 31.8°C at 100 epochs versus 32.4°C in the true data (d), and 32.0°C at 300 epochs versus 32.4°C in the true data (f). This persistent underestimation, along with a residual maximum error of $\Delta T \approx 8.54°C$ after 300 epochs, indicates that the chosen hyperparameters fail to integrate the boundary conditions effectively into the final solution. These results provide indirect support for the use of a higher boundary weight λ_2=0.5 as our experiment for Washington D.C. city. A stronger boundary constraint would likely counterbalance the overemphasis on physics, enforce stricter adherence to the boundaries, and produce predictions more closely aligned with the observed thermal patterns.

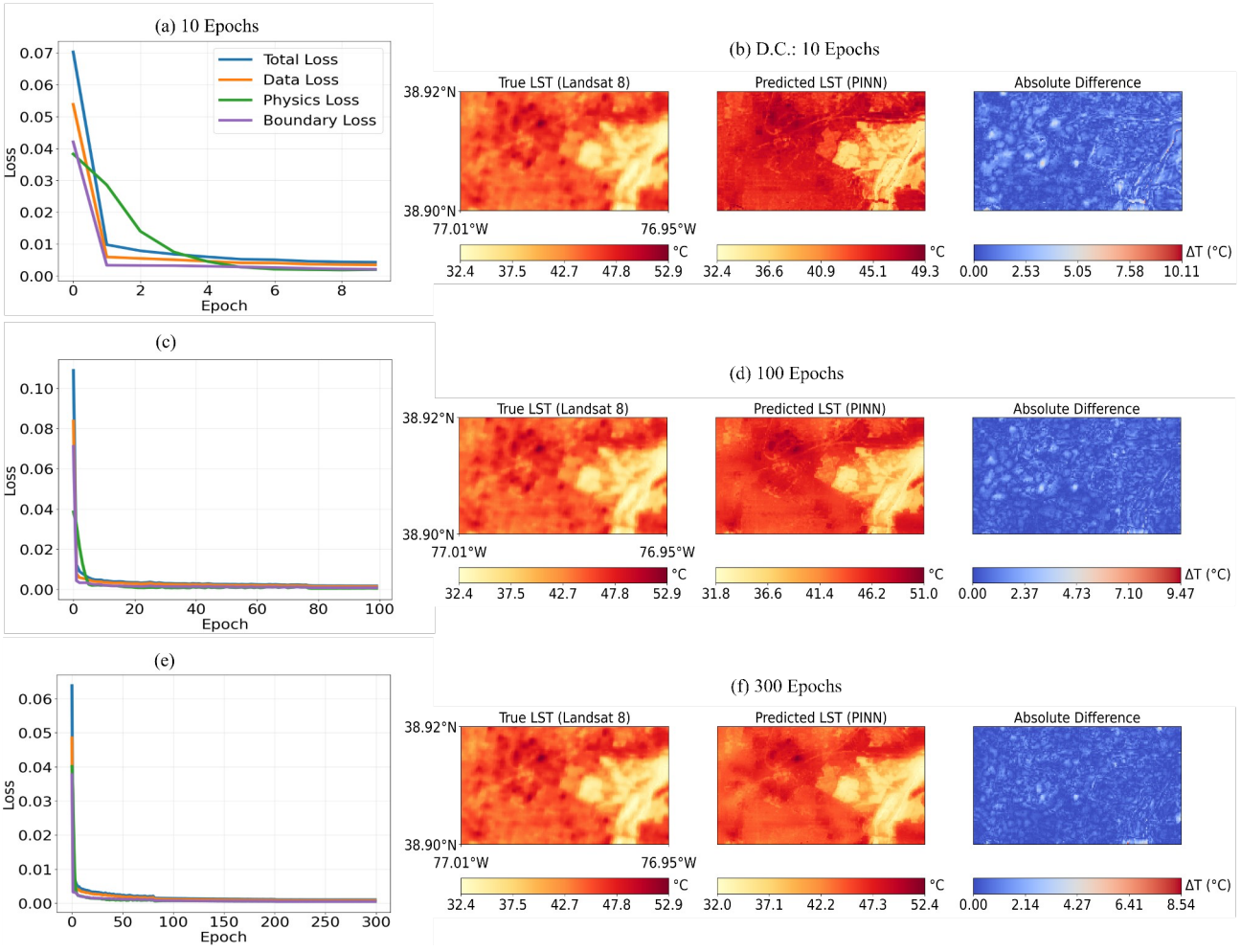

Appendix A. 2. *D.C. model performance with boundary weight* $\lambda_2 = 0.3$: *physics loss dominance (a, c, e) causes underpredicted LST and spatial errors (b, d, f), demonstrating suboptimal results versus* $\lambda_2 = 0.5$

Appendix A.3 demonstrates the critical role of physics-informed loss weight $\lambda_1$in modelling Bologna's LST, revealing that excessive or insufficient λ_1 degrades performance while $\lambda_1 = 0.1$ (implied as the optimal value in Table 2) achieves balance.

In subfigure (a) the physics loss ($\lambda_1 = 0.01$) is a dominant component of the total loss, despite its low absolute magnitude. This indicates that the physical constraints are not being sufficiently enforced. The consequence is visible in the prediction map (b), which shows spatially distorted thermal patterns and a failure to resolve fine-grained features such as urban heat islands, culminating in a significant maximum error ($\Delta T = 6.67°C$). Conversely, when λ_1 is raised to 1.0 and 1.5 (subfigures c and e), the physics loss becomes overwhelmingly dominant. This forces the model to over-prioritise the physical constraints at the expense of fitting the observational data. The resulting predictions (d and f) display a systematic overestimation of LST. For instance, at $\lambda_1 = 0.1$ the model predicts a maximum temperature of 49.7°C compared to the true maximum 49.3°C, suggesting it is amplifying unrealistic thermal extremes to comply with the physics loss. The error maps (b, d, f) collectively demonstrate that a value of $\lambda_1 = 0.1$ (in our result) —inferred from this trend—avoids both the pattern distortion seen at low weights and the temperature overestimation seen at high weights. This analysis validates the selection of $\lambda_1 = 0.1$ for Bologna, as it successfully enforces physical plausibility without

overwhelming the data fidelity, thereby enabling accurate LST prediction.

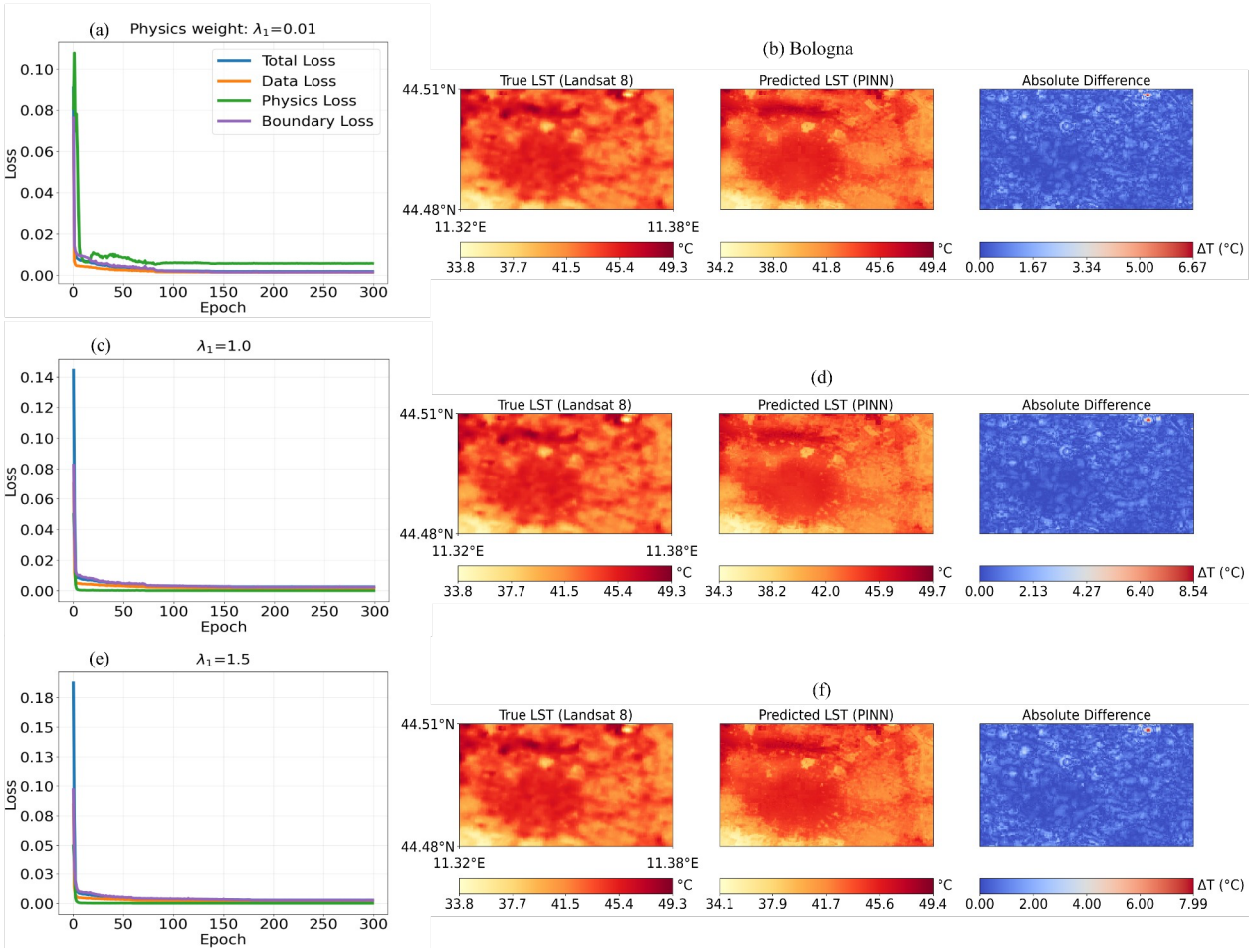

Appendix A. 3. *Bologna model performance with varying physics weight* (λ_1): (a) λ_1= 0.01 *distorts spatial patterns (b) while* $\lambda_1 \geq$ *1.0 overestimates LST (d, f).*

Appendix A.4 systematically evaluates the physics-informed loss weight (λ_1) for Washington D.C., demonstrating that performance degrades when the physics constraints are either under- or over-weighted. The analysis confirms that λ_1= 0.1 achieves the necessary balance for accurate modelling.

In subfigure (a), where λ_1= 0.01, the physics loss remains a dominant component of the total loss despite its low absolute value, indicating that the physical constraints are not being adequately enforced during training. This leads to spatially biased predictions in (b), where the model fails to capture the observed thermal heterogeneity. For instance, the predicted minimum LST of 32.2°C does not fully resolve the variation present in the true data (minimum 32.4°C), resulting in a high maximum error (ΔT = 10.59°C) and distorted urban heat patterns. Conversely, for λ_1 = 1.0 and 1.5 (subfigures c and e), the excessive weight on the physics term over-constrains the solution. This leads to a systematic underestimation of temperatures, with predicted LST minima dropping to 29.6°C (d) and 31.7°C (f) —both below the true minimum of 32.4°C. Despite this strong physical constraint, the maximum error remains high (9.77°C and 9.89°C). The colour bar ranges in (d) and (f) clearly reveal this cooling bias, showing that the model sacrifices data fidelity to enforce physical consistency.

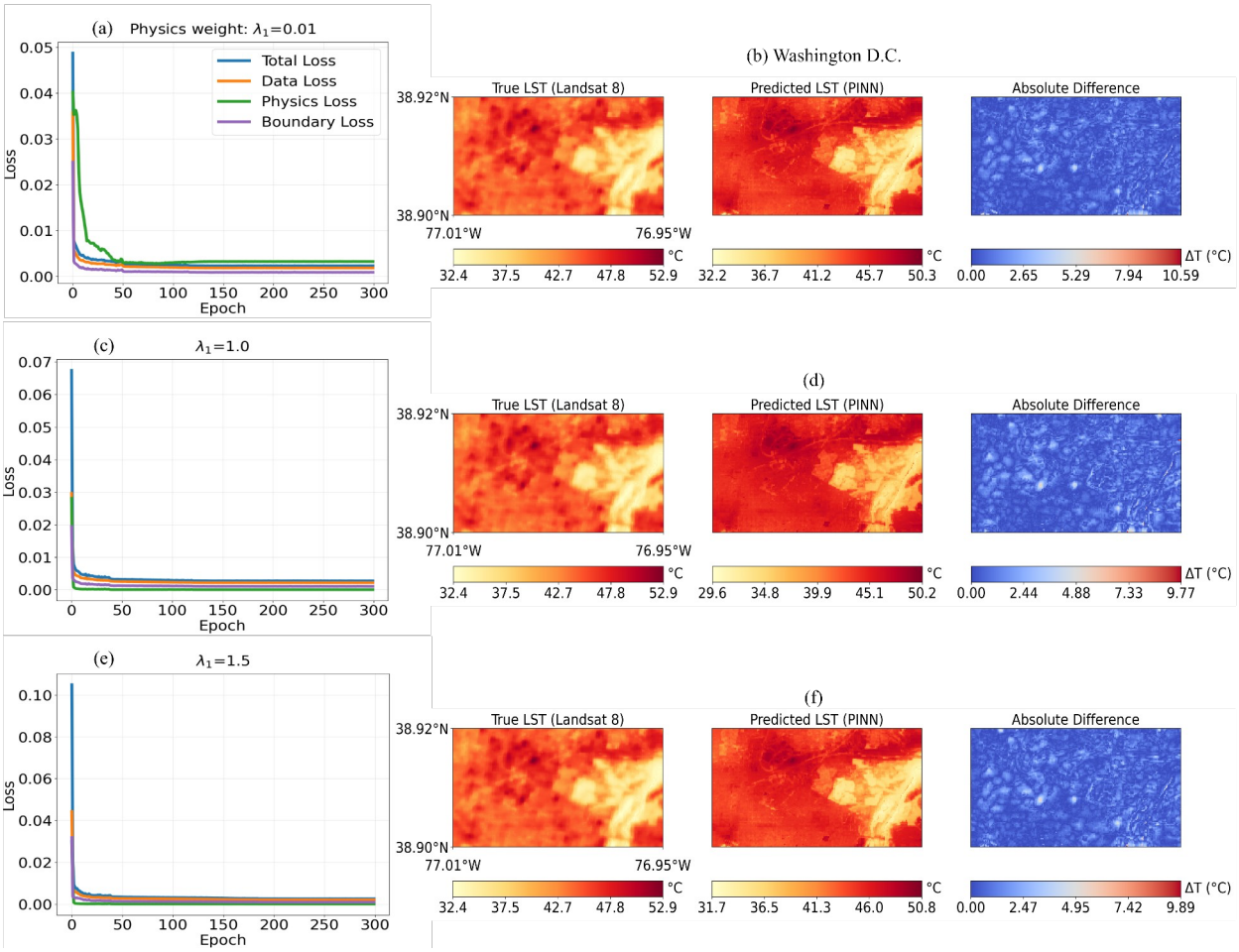

Appendix A. 4. *Washington D.C. model response to physics weight (λ_1): (a) λ_1= 0.01 causes spatial bias in (b); while $\lambda_1 \geq 1.0$ underestimates minimum predicted LST (d, f).*

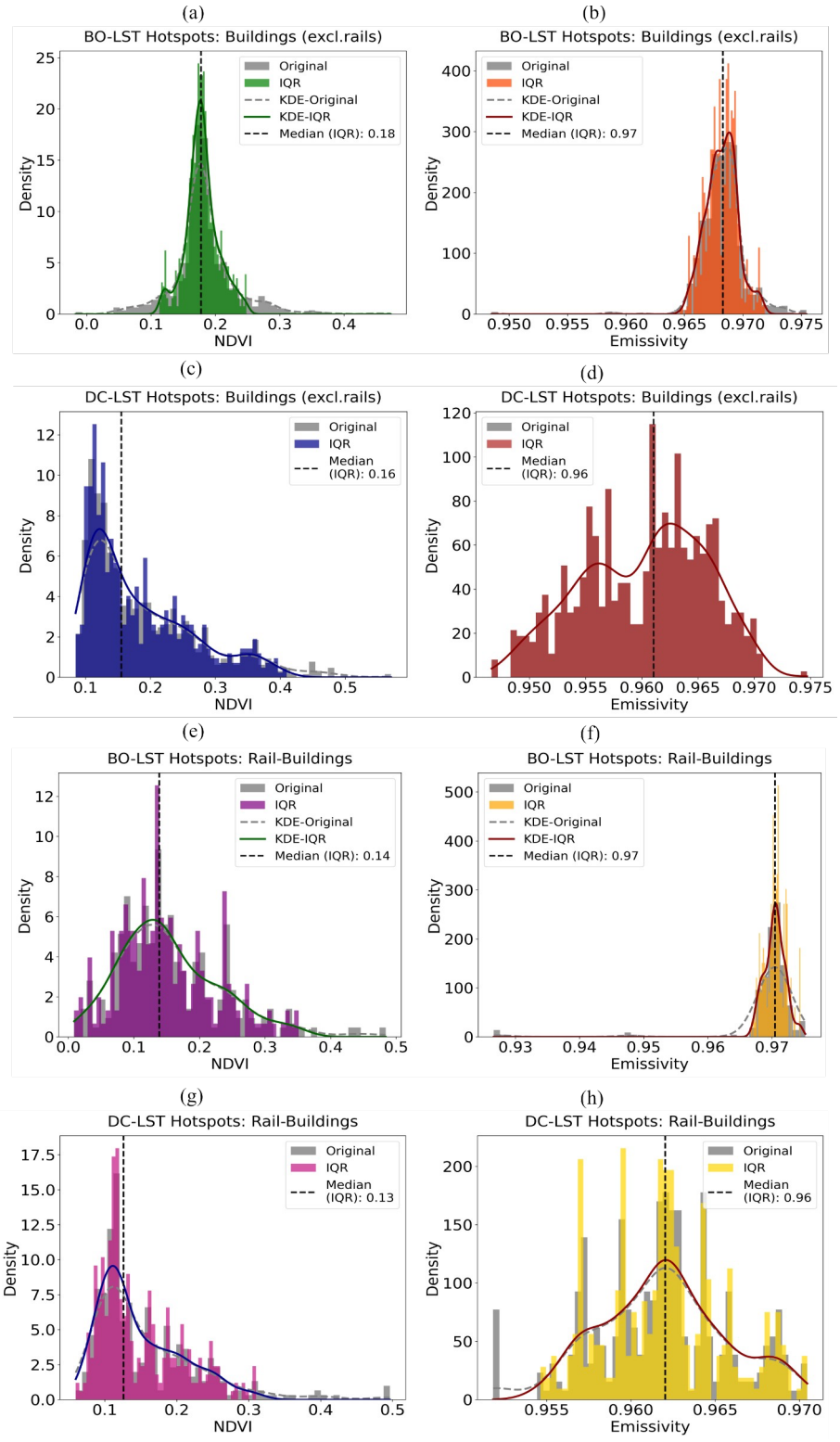

Appendix B. *Density distributions of NDVI (a, c, e, g) and emissivity (b, d, f, h) for LST hotspots in Bologna (BO) and D.C. (DC), comparing buildings excluding rails and rail-inclusive areas.*

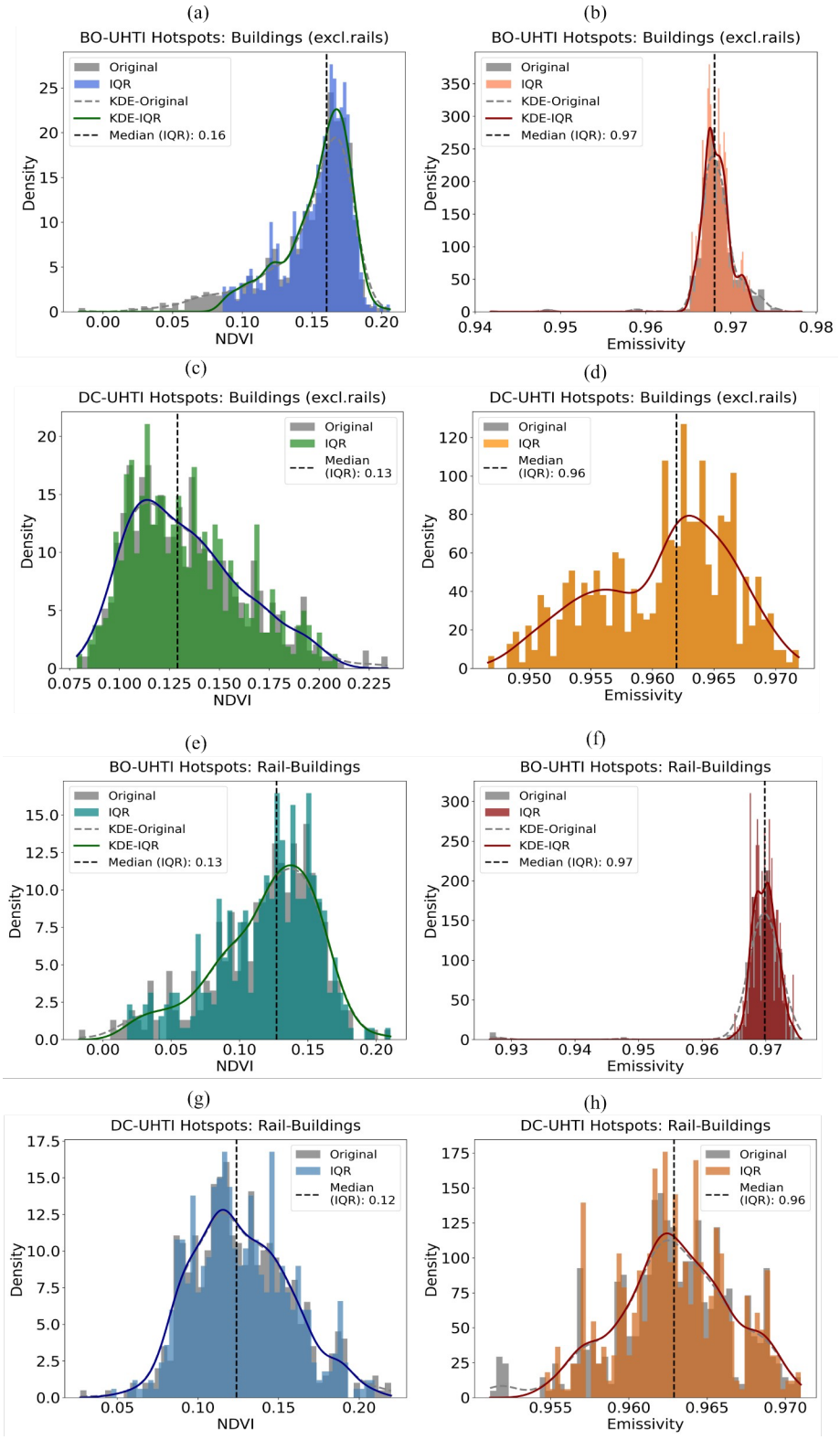

Appendix C. *UHTI hotspots reveal reduced vegetation signatures: NDVI (a, c, e, g) and emissivity (b, d, f, h) density distributions for Bologna (BO) and D.C. (DC), contrasting rail-excluded vs. rail-inclusive urban zones*

Table A2: NDVI and Emissivity with LST Hotspots

City	Building type	Variable	Total Pixels	Outlier Pixels	Pixels after IQR	Min (after IQR)	Max (after IQR)
Bologna	Buildings (excl. rails)	NDVI	1108	157	951	0.113	0.248
		Emissivity	1108	45	1063	0.965	0.972
	Rail-buildings	NDVI	225	4	221	0.009	0.351
		Emissivity	225	9	216	0.967	0.974
Washington D.C.	Buildings (excl. rails)	NDVI	667	16	651	0.085	0.410
		Emissivity	667	0	667	0.947	0.975
	Rail-buildings	NDVI	347	14	333	0.060	0.310
		Emissivity	347	10	337	0.955	0.970

Table A3: NDVI and Emissivity with UHTI Hotspots

City	Building type	Variable	Total Pixels	Outlier Pixels	Pixels after IQR	Min (after IQR)	Max (after IQR)
Bologna	Buildings (excl. rails)	NDVI	1116	76	1040	0.086	0.206
		Emissivity	1116	73	1043	0.965	0.972
	Rail-buildings	NDVI	335	4	331	0.018	0.210
		Emissivity	335	8	327	0.965	0.974
Washington D.C.	Buildings (excl. rails)	NDVI	624	6	618	0.079	0.209
		Emissivity	624	0	624	0.947	0.972
	Rail-buildings	NDVI	516	5	511	0.046	0.210
		Emissivity	516	12	504	0.955	0.971